

# Airfoil Dynamic Stall and Rotorcraft Maneuverability

WILLIAM G. BOUSMAN

*Army/NASA Rotorcraft Division  
Aeroflightdynamics Directorate (AMRDEC)  
US Army Aviation and Missile Command  
Ames Research Center, Moffett Field, California*

## SUMMARY

The loading of an airfoil during dynamic stall is examined in terms of the augmented lift and the associated penalties in pitching moment and drag. It is shown that once stall occurs and a leading-edge vortex is shed from the airfoil there is a unique relationship between the augmented lift, the negative pitching moment, and the increase in drag. This relationship, referred to here as the dynamic stall function, shows limited sensitivity to effects such as the airfoil section profile and Mach number, and appears to be independent of such parameters as Reynolds number, reduced frequency, and blade sweep. For single-element airfoils there is little that can be done to improve rotorcraft maneuverability except to provide good static  $c_{l_{max}}$  characteristics and the chord or blade number that is required to provide the necessary rotor thrust. However, multi-element airfoils or airfoils with variable geometry features can provide augmented lift in some cases that exceeds that available from a single-element airfoil. The dynamic stall function is shown to be a useful tool for the evaluation of both measured and calculated dynamic stall characteristics of single-element, multi-element, and variable geometry airfoils.

## NOMENCLATURE

$a_p, b_i$	polynomial coefficients for $c_{l_{max}}$ , $i = 0, 1, 2$	$C$	section chord force, lb
$a_s$	speed of sound, ft/sec	$C_L$	mean blade lift coefficient
$b$	number of blades	$C_{P_0}$	profile power coefficient
$c$	blade chord, ft	$C_T$	thrust coefficient
$c_c$	section chord force coefficient	$e$	root cutout radius, ft
$c_d$	section drag coefficient	$k$	reduced frequency
$c_{d_{max}}$	maximum drag coefficient in dynamic stall, Fig. 6	$M$	Mach number; section moment, ft-lb/ft
$c_{d_0}$	section drag coefficient at zero lift	$M_a$	blade aerodynamic moment, ft-lb
$c_l$	section lift coefficient	$M_c$	Mach number normal to leading edge
$c_{l_{max}}$	maximum lift coefficient in dynamic stall, Fig. 6	$M_{sp}$	fixed-system control moment, ft-lb
$\bar{c}_l$	static $c_{l_{max}}$	$M_T$	hover tip Mach number
$\hat{c}_l$	corrected section lift coefficient, eq (10)	$M_\infty$	free stream Mach number
$c_m$	section moment coefficient	$q$	dynamic pressure, lb/ft <sup>2</sup>
$c_{m_{min}}$	minimum moment coefficient in dynamic stall, Fig. 6	$r$	blade radial location, ft; correlation coefficient
$c_n$	section normal force coefficient	$r_{sp}$	swashplate moment radius, ft
		$R$	blade radius, ft
		$Re$	Reynolds number
		$T$	rotor thrust, lb

$T_b$	blade thrust, lb
$V(r, \psi)$	section velocity, ft/sec
$V_H$	maximum level flight speed, ft/sec
$V_T$	hover tip speed, ft/sec
$\alpha$	section angle of attack, deg
$\alpha_0$	mean angle of attack, eq (7), deg
$\alpha_1$	alternating angle of attack, eq (7), deg
$\Delta c_l$	Mach number correction for lift coefficient, eq (11)
$\theta$	airfoil deformation angle, eq (21)
$\Lambda$	sweep angle, deg
$\mu$	advance ratio
$\mu_v$	viscosity, lb-sec/ft <sup>2</sup>
$\rho$	density, slugs/ft <sup>3</sup>
$\sigma$	solidity; standard deviation
$\psi$	azimuth angle, deg
$\omega$	oscillation frequency, 1/sec
$\Omega$	rotor speed, 1/sec
Superscript:	
*	limit condition

## INTRODUCTION

The thrust capability of a helicopter rotor is directly related to the lift capability of the blade airfoil section. In forward flight the thrust of one blade can be expressed as

$$T_b(\psi) = \frac{1}{2} \rho c V_T^2 \int_e^R c_l(r, \psi) \left[ \frac{r}{R} + \mu \sin \psi \right]^2 dr \quad (1)$$

and the thrust of the rotor must be summed over the  $b$  blades. In hover, eq (1) can be simplified if a mean blade lift coefficient,  $C_L$ , is defined that is not dependent upon the radius,  $r$ , or the blade azimuth,  $\psi$

$$T_b = \frac{1}{6} \rho c R V_T^2 C_L \quad (2)$$

The blade thrust can then be summed over the number of blades and, in terms of the thrust coefficient,  $C_T/\sigma$ , the classical result is obtained

$$\frac{C_T}{\sigma} = \frac{1}{6} C_L \quad (3)$$

For a helicopter with  $M_T = 0.65$  and with  $C_L$  defined at  $0.75R$ , then for a modern airfoil such as the Sikorsky SC1095, the maximum  $C_L$  is about 1.1 (Ref. 1). In this case, the maximum rotor thrust that can be expected is  $C_T/\sigma \sim 0.18$ .

In forward flight, the airfoil lift coefficient in eq (1),  $c_l(r, \psi)$ , will be affected by the advance ratio and, if it is assumed that roll moment balance must be maintained at the rotor thrust limit (Ref. 2), then

$$\frac{C_T}{\sigma} = \frac{C_L}{6} \left( \frac{1 - \mu^2 + 9\mu^4/4}{1 + 3\mu^2/2} \right) \quad (4)$$

McHugh and his colleagues have measured the thrust capability of a 10-foot diameter CH-47B model rotor in the Boeing 20- by 20-foot V/STOL Wind Tunnel (Ref. 3, 4). These measurements are particularly useful as the rotor was designed with sufficient structural strength that the true aerodynamic thrust limit could be identified, that is, the collective pitch angle where the rotor thrust reached its maximum value. The rotor thrust limit from the Boeing tests is shown in Fig. 1 and is compared to the limit calculated from eq (4), assuming  $C_L = 0.94$ .

The problem of relating rotor thrust capability to airfoil section characteristics becomes more difficult than suggested by eq (1) when it is recognized that the rotor thrust limit is not dependent upon the maximum static airfoil lift, but that there is an unsteady or dynamic component that increases the thrust capability (Ref. 5). Measurements of the rotor thrust of a full-scale H-21 rotor in the 40- by 80-Foot Wind Tunnel, by McCloud and McCullough (Ref. 6), demonstrated that the rotor was able to provide more thrust than would be calculated using just the static airfoil lift coefficient (Ref. 5). This additional lift, what is now referred to as dynamic stall, has been the subject of extensive research over the past 40 years (Ref. 7, 8).

A fundamental problem for the rotor designer, then, is to what degree does the airfoil design affect the rotor's thrust capability and, probably more important, the increased pitching moment and power that accompanies the augmented lift associated with dynamic stall. The McCloud and McCullough experiments (Ref. 6) provided a partial answer in that they demonstrated that a second rotor, with improved static  $c_{l_{max}}$  capabilities, also improved the overall rotor thrust. Their measurements showed that the increment in rotor thrust for the second rotor was approximately proportional to the increase in the static  $c_{l_{max}}$  of the improved airfoil.

A great deal of fundamental information relating to dynamic stall has been obtained since the first critical experiments of Ref. 6, particularly from wind tunnel tests

of two-dimensional airfoil sections. Notable among these tests are the experiments performed by McCroskey and his colleagues (Refs. 9–11) wherein they examined the dynamic stall characteristics of eight airfoils in a comparative fashion in the 7- by 10-Foot Wind Tunnel at NASA Ames Research Center. The purpose of the present study is to use the Ames test data to better understand the airfoil design characteristics that affect the augmented lift in dynamic stall and the associated moment and drag penalties. These data, as well as other test data, will be used to understand what parameters most strongly influence the dynamic stall loading. A comparison will be drawn between dynamic stall loading as obtained from two-dimensional wind tunnel data and from recent flight tests of a UH–60A (Ref. 12). Based on the various test data some general comments will be provided as concerns design for rotorcraft maneuverability based on airfoil dynamic stall characteristics on single-element airfoils. The study will conclude with an examination of the possibility of enhanced maneuverability using multi-element airfoils or airfoils with variable geometry.

## COMPARATIVE AIRFOIL TESTS

### Ames Test Program

McCroskey and his colleagues (Refs. 9–11) tested eight airfoils in the NASA-Ames 7- by 10-Foot Wind Tunnel. Each airfoil was tested using the same dynamic rig and, in general, the same range of test conditions was covered. The eight profiles are shown in Fig. 2.

The first of the eight profiles, the NACA 0012, is representative of the first generation of airfoils used for helicopters and has a symmetric section. With slight modifications this section was used for Sikorsky Aircraft's H–34 family of helicopters, which first flew in 1954.

The AMES–01 airfoil was specifically designed for use in helicopters and is representative of a second generation of airfoils. It has not been used, however, in an operational helicopter.

The Wortmann FX 69–H–098 airfoil is also a second-generation airfoil and was designed for Bell Helicopter Textron for use in some of their two-bladed helicopters. For application to flight vehicles the airfoil was modified to add camber near the trailing edge to shift the section moment to zero and the modified airfoil is different from the airfoil tested at NASA Ames. The modified airfoil has been used in the 214 series of helicopters (214A, 214B, 214C, and 214ST) and also the AH–1T and AH–1W helicopters.

The Sikorsky-designed SC1095 airfoil is another second-generation airfoil and is used on both their UH–60A Black Hawk and the S–76. The airfoil is used both inboard and outboard on the UH–60A with a modified section, the SC1094 R8, used over the mid-portion of the blade. For the S–76, the SC1095 is used only on the outer portion of the blade. Inboard the SC1094 R8 is used for the mid-portion and transitions to the SC1013 R8 near the blade root (Ref. 13). The SC1095 airfoil as used on the S–76 includes a –3 deg reflexed tab, to reduce the negative moment on this section, and this is different from the airfoil tested at Ames. The SC1095 on the UH–60A does not include a tab and is identical to the airfoil evaluated in the Ames program.

The Hughes Helicopters HH–02 profile was tested with a –5 deg tab to balance out the pitching moment from the camber of the airfoil. This second-generation airfoil is used on the AH–64A and AH–64D helicopters.

The VR–7 profile was developed by Boeing Vertol and was tested with a –3 deg tab in the Ames tests. This airfoil is used on the current Boeing CH–47D, but with a –6 deg tab. The VR–7 is also considered a second-generation airfoil.

The NLR–1 profile was designed specifically for improved transonic performance and has been test flown on an instrumented AH–1G helicopter (Ref. 14, 15). Although it has good high Mach number performance its low-speed characteristics are unsatisfactory and it has never been used for a production helicopter.

The last profile, the NLR-7301, is representative of a supercritical, fixed-wing section. Compared to the other seven airfoils, it is characterized by a large leading-edge radius and large aft camber which results in large negative pitching moments at all angles of attack. It is not considered suitable for use in helicopter applications, but was included in the test program to better understand the dynamic stall characteristics of fixed-wing airfoil sections with significantly different leading edge geometries.

The airfoil chord for all of the eight profiles was 24 in. The airfoil was mounted vertically in the test section of the 7- by 10-Foot Wind Tunnel such that the airfoil spanned the shorter dimension. Thus the height to chord ratio was 5.0, based on the 10-foot width of the tunnel and the width to chord ratio was 3.5. Fifteen pressure transducers were mounted on the upper surface, ten were placed on the lower surface, and a single transducer was installed at the airfoil leading edge. The measured pressures were integrated to obtain the section

forces,  $c_n$  and  $c_c$ , and the section moment,  $c_m$ . The measured angle of attack of the airfoil was used to convert these coefficients to the wind tunnel axes.

$$\begin{aligned} c_l &= -c_c \sin \alpha + c_n \cos \alpha \\ c_d &= c_c \cos \alpha + c_n \sin \alpha \end{aligned} \quad (5)$$

The  $c_d$  calculated in this manner does not include the viscous drag, of course. The uncertainty in the section forces and moment in deep stall has been estimated (Ref. 9) as

$$\begin{aligned} c_l &= \pm 0.20 \\ c_d &= \pm 0.05 \\ c_m &= \pm 0.10 \end{aligned} \quad (6)$$

Dynamic stall data were obtained in the Ames tests by oscillating the airfoil in angle of attack around a mean value. The airfoil motion was defined as

$$\alpha(\omega t) = \alpha_0 + \alpha_1 \sin \omega t \quad (7)$$

The lift, drag, and section moments for these conditions were provided in Ref. 10 for each of the eight airfoils. The number of test conditions, as defined by the mean angle of attack,  $\alpha_0$ , the alternating angle of attack,  $\alpha_1$ , the reduced frequency,  $k$ , and the Reynolds and Mach numbers range from 49 for the Wortmann FX 69-H-098 to 121 for the NACA 0012. Not all of these test points are included here. For the NACA 0012 airfoil, a number of cases were for quasi-static rather than dynamic stall conditions, that is, the reduced frequency was approximately zero ( $k < 0.005$ ), and these 21 conditions are not included. For the NLR-1 airfoil, a set of test cases was run with  $\alpha_0 = -2$  deg and  $\alpha_1 = 10$  deg and, therefore, dynamic stall occurred for negative lift conditions. These eight test cases have also been excluded from the comparisons shown here. Finally, 13 test conditions for the NLR-7301 are excluded where  $\alpha_0$  was set close to the static stall angle, and small values of the alternating angle of attack,  $\alpha_1 = 2$  deg, were used to better understand this airfoil's flutter characteristics. None of these conditions indicated the shedding of a dynamic stall vortex, and in some cases the airfoil remained stalled for the full cycle.

The Reynolds and Mach numbers for the test conditions for the eight airfoils are shown in Fig. 3. The maximum test section velocity is approximately  $M = 0.3$  and this provides a Reynolds number of about four million. As this tunnel operates with the stagnation pressure vented to the atmosphere, the Reynolds number is proportional to the Mach number as shown in the figure. Reynolds number is also proportional to Mach number for a helicopter in flight and this proportionality is indicated in Fig. 3 for a number of the helicopters that

use the indicated airfoil sections. The Reynolds number depends upon Mach number as

$$Re = \frac{\rho c a_s}{\mu_v} M \quad (8)$$

The helicopter characteristics shown in Fig. 3 are calculated assuming flight at a pressure altitude of 3000 feet on a standard day. In this case  $\rho = 0.002175$  slug/ft<sup>3</sup>,  $a_s = 1105$  ft/sec, and  $\mu = 3.738 \times 10^{-7}$  lb-sec/ft<sup>2</sup>.

The 24 in. chord used in the Ames tests provides reasonably representative Reynolds numbers for these airfoils over the Mach number test range. Note, however, that these Mach numbers cover only the lower end of the flight vehicle range where Mach numbers typically exceed 0.8 or 0.9 near the tip of the blade at high speed.

The mean and alternating angles of attack are shown in Fig. 4 for the eight airfoils. Most of the test points were for alternating angles of 5 and 10 deg, and mean values of 5, 10, and 15 deg.

The reduced frequencies for the Ames tests are shown as a function of Mach number in Fig. 5 for the eight airfoils. For most of the airfoils the reduced frequency ranged from about 0.025 to 0.20. For the NACA 0012, the upper range of reduced frequency was extended to values as high as 0.28.

Section force and moment time histories are provided in Ref. 10 for each airfoil and each test case. Figure 6 shows an example of the lift, drag, and moment loops for a test condition for the NACA 0012 that represents deep stall. Indicated on this figure are the maximum lift point, the maximum drag point, and the minimum moment point for the oscillation. These extrema occur at slightly different angles of attack and are, therefore, not coincident in time. However, they are each related to the passage of the dynamic stall vortex along the airfoil and are representative of the maximum loading that occurs during a dynamic stall cycle.

The extrema from the Ames tests are shown in Figs. 7 and 8 for all of the airfoils. Figure 7 shows the maximum  $c_l$  as a function of the minimum  $c_m$ , and Fig. 8 shows the maximum  $c_l$  as a function of the maximum  $c_d$ . The maximum lift, maximum drag, and minimum moment are related by the dynamic stall vortex that is shed from near the leading edge during deep stall. However, these extrema do not occur simultaneously, and the functional behavior shown in Figs. 7 and 8 represents the envelope of loading rather than a simultaneous load.

Included in Fig. 7 are the measured static stall characteristics at  $M = 0.3$  from Ref. 9. Below stall there is little variation in pitching moment with lift, as

expected. Most of the airfoils have very low steady moments so as to avoid high loads in the control system. The FX 69-H-098 and the SC1095 both show steady moments as large as  $-0.03$  or  $-0.04$  but the other profiles are closer to zero. The NLR-7301, however, shows a significantly larger steady moment than the helicopter sections, about  $-0.18$ . For a fixed-wing section, where the moment is reacted by the tailplane, negative moments of this size do not represent a serious problem. For helicopters, however, where the moments must be reacted by the control system, it is necessary to avoid large aerodynamic moments.

In Fig. 8, the static drag measurements are included in this figure as a dotted line and the drag determined from wake measurements is shown by a solid line. The latter measurements include viscous drag effects. The steady drag measurements shown here were obtained at  $M = 0.3$ .

The most obvious feature observed in Figs. 7 and 8 is that dynamic stall is characterized as a fairly uniform or monotonic function. To a degree this result is expected as most of the test points in these figures ( $c_m < -0.15$  and  $c_d > 0.4$ ) are associated with one or more dynamic stall vortices that are shed from near the airfoil leading edge. The dynamic stall vortices, once formed, clearly dominate the lift, the drag, and the moment and a universal relationship is exhibited.

A second feature observed in Figs. 7 and 8 is that as the dynamic moments and drag approach zero, the dynamic lift approaches its static maximum value as well. This characteristic is reasonably to be expected as at near-zero values of moment and drag, no vortex shedding is associated with the unsteady airfoil motion and the unsteady lift is not much greater than the static lift.

The data from Figs. 7 and 8 are repeated in Figs. 9 and 10 and are separated into cases with and without a boundary layer trip. The untripped data are fitted with a 2nd-order polynomial as shown by the dashed lines. The polynomials are defined as

$$\begin{aligned} c_l &= a_0 + a_1 c_m + a_2 c_m^2 \\ c_l &= b_0 + b_1 c_d + b_2 c_d^2 \end{aligned} \quad (9)$$

The polynomials in eq (9) are referred to here as the “dynamic stall functions.” The tripped boundary layer data were excluded from the fit as it appears that these data have a small but significant influence on the dynamic stall function. The effect of the boundary layer trip is discussed in greater detail in a subsequent section. The coefficients of the fitting polynomials are shown in Tables 1 and 2 along with two measures of dispersion: the coefficient of determination,  $r^2$ , and the standard deviation,  $\sigma$ .

The polynomial fits obtained in Figs. 9 and 10 provide a fairly good representation of the dynamic stall behavior with the exception, perhaps, of the fixed-wing section, the NLR-7301, which shows more scatter than the other airfoils.

The dynamic stall functions, based on  $c_m$  and  $c_d$ , are compared for the seven helicopter sections in Fig. 11. The polynomial fits are from Tables 1 and 2. At values near zero  $c_m$  or  $c_d$ , the lift is close to the static  $c_{l_{max}}$ . As the section achieves higher  $c_l$  in dynamic stall, the moment becomes more negative and the drag more positive. The NACA 0012 airfoil defines a rough lower bound for the dynamic stall function over most of the moment and drag values, and each of the second generation airfoils shows improved capability with  $\Delta c_l$  of 0.2 to 0.5. Some of the second-generation airfoils show an improvement in the intercept, either  $a_0$  or  $b_0$ , most notably the VR-7 with the  $-3$  deg tab. Other profiles, however, show the biggest improvement at higher lift, such as the AMES-01 and the HH-02. The NLR-1 shows good performance at moderate lift coefficients, but near zero  $c_m$  or  $c_d$ , this airfoil shows reduced dynamic lift and does not even match its static  $c_{l_{max}}$ .

Another way to compare the dynamic stall functions is separate out the static portion. This comparison is shown for the seven helicopter sections in Fig. 12 by plotting  $c_l/a_0$  and  $c_l/b_0$  as functions of  $c_m$  and  $c_d$ . Except for the NLR-1, the dynamic stall functions for these airfoils are very similar. Based on this comparison, the AMES-01 and HH-02 airfoils appear to have the best performance in the region with deep dynamic stall.

A comparison of the  $a_0$  and  $b_0$  intercepts in Tables 1 and 2 shows that, in general, the intercepts for each airfoil agree closely. This result is expected as the dynamic stall behavior shown here, that is, the peak loading that is seen in lift, moment, and drag are all the result of the same unsteady aerodynamic phenomena.

There appears to be a rough correspondence between the  $a_0$  and  $b_0$  intercepts from the dynamic stall function and the measured static  $c_{l_{max}}$  as shown in Fig. 13. A linear regression has been computed for the relationship in Fig. 13 and the slopes relating the  $a_0$  and  $b_0$  intercepts are 1.97 and 1.83, respectively, and the intercepts are  $-1.28$  and  $-1.13$ . However, the functional relationship shown here is strongly affected by the poor dynamic performance of the NLR-1 airfoil at near-zero values of moment and drag and it is probably best to avoid reading too much into the fitted line. It is sufficient to conclude that an airfoil with a better static  $c_{l_{max}}$  will also provide better dynamic stall performance—a conclusion reached by McCloud and McCullough over 40 years ago (Ref. 6).

Table 1. – 2nd order polynomial fit of dynamic stall function, lift as a function of moment.

AIRFOIL	$a_0$	$a_1$	$a_2$	$r^2$	$\sigma$
NACA 0012	1.439	-0.791	2.232	0.81	0.14
AMES-01	1.627	-0.361	4.210	0.85	0.13
FX 69-H-098	1.530	-0.107	3.519	0.84	0.12
SC1095	1.582	-0.532	2.869	0.95	0.07
HH-02	1.474	-0.643	4.054	0.95	0.08
VR-7	1.672	-0.229	3.773	0.84	0.14
NLR-1	1.184	-2.721	0.026	0.93	0.10
NLR-7301	1.618	-2.392	-0.973	0.53	0.15

Table 2. – 2nd order polynomial fit of dynamic stall function, lift as a function of drag.

AIRFOIL	$b_0$	$b_1$	$b_2$	$r^2$	$\sigma$
NACA 0012	1.371	0.741	0.156	0.82	0.14
AMES-01	1.571	0.679	0.368	0.86	0.12
FX 69-H-098	1.516	0.238	0.649	0.85	0.12
SC1095	1.485	0.971	0.044	0.93	0.08
HH-02	1.373	0.997	0.129	0.93	0.09
VR-7	1.673	0.402	0.448	0.86	0.14
NLR-1	1.208	0.990	0.332	0.91	0.11
NLR-7301	1.769	1.010	-0.361	0.48	0.16

A review of the airfoil dynamic stall time histories in Ref. 10 shows qualitative differences between the various test conditions. These time histories have been examined and a judgment has been made as to whether, (1) a dynamic stall vortex is not evident in the data, (2) a single dynamic stall vortex is evident and is clearly shed from the airfoil, and (3) two dynamic stall vortices are shed. In most cases these distinctions are clear, but there are also situations where the time history is ambiguous and the classification may not be satisfactory. The dynamic stall data points, each assigned to one of the three classifications, are shown in Figs. 14 and 15 and are compared with the polynomial fits of Tables 1 and 2. This comparison shows that for the most part, those conditions where dynamic lift is only slightly higher than the airfoil maximum static lift coefficient are

generally characterized by light stall conditions where no dynamic stall vortex is apparent. For more severe loading conditions, a single dynamic vortex is observed, while for the most severe loading, two dynamic stall vortices are seen. The test points with two dynamics stall vortices represent those conditions in the Ames tests that had the greatest excursions in lift, moment, and drag.

### Comparison of Ames Test Data with Other Sources

An examination of dynamic stall data from the eight airfoils tested in the Ames 7- by 10-Foot Wind Tunnel (Refs. 9-11) shows that the loading in lift, moment, and drag is very similar for the seven helicopter

airfoil sections over a wide range of parameters. It is expected that these results should be supported by dynamic stall test results from other facilities and comparisons are shown in this section between the Ames data and a number of other data sources for the NACA 0012, SC1095, VR-7, and NLR-1 airfoils.

NACA 0012 dynamic stall test data were obtained in the UTRC Main Wind Tunnel in an investigation whose primary focus was to examine the effects of blade sweep (Ref. 16). However, this experiment also included unswept data as a baseline, and it is these unswept data that are examined here. The effects of sweep are discussed in a later section. Twelve pressure transducers were installed on the upper surface of the airfoil and eight on the lower surface, both in Gaussian arrays. Lift, drag, and moment were obtained by integrating the measured pressures and the  $c_n$  and  $c_c$  coefficients were converted to wind tunnel axes using eq (5). The test conditions and the maximum  $c_l$  and  $c_d$ , and minimum  $c_m$  are compared with the Ames tests results in Fig. 16. The Ames test data are limited to those values used to determine the polynomial fits in Tables 1 and 2.

Most of the UTRC data were obtained for  $M = 0.3$ , but a few values were also obtained at  $M = 0.1$ . The range of alternating and mean amplitudes and the reduced frequencies tested generally overlap the Ames test conditions. The maximum  $c_l$  and minimum  $c_m$  values, and the maximum  $c_l$  and  $c_d$  values obtained from the UTRC dynamic stall loops compare quite well with the polynomial fit obtained from the Ames data, generally being within  $\pm 1\sigma$  of the Table 1 and 2 polynomials. Three or four values at high lift are well outside the Ames data scatter, however. These high lift points are the values obtained at  $M = 0.1$  and it is not clear whether the low Mach number is a contributing influence.

Dynamic stall data have been obtained for the SC1095 (and SC1094 R8) airfoil using the Ref. 16 test rig in the UTRC Main Wind Tunnel, but these data have not been published. However, a very limited number of  $c_l$  and  $c_m$  loops have been shown by Gangwani (Ref. 17), and these are compared with the Ames test data for the SC1095 airfoil in Fig. 17.

The five UTRC test conditions were obtained for  $M = 0.3$  and generally fall within the range of the Ames test conditions. The  $c_l$  and  $c_m$  extrema are slightly below the Ames polynomial fit and two of the points are slightly outside the  $\pm 1\sigma$  bounds.

Two sources of dynamic stall data have been examined for the VR-7 airfoil. The first data set is from the Centre D'Essais Aeronautique de Toulouse (CEAT) wind tunnel in Toulouse, France, and was obtained under

the auspices of the U.S./France Memorandum of Understanding for Cooperative Research in Helicopter Aeromechanics. A general description of the test procedures used with this wind tunnel and test rig are provided in Ref. 18. The second data set is from the Ames water tunnel (Ref. 19). The CEAT data were obtained in a conventional atmospheric wind tunnel using a model with a 40-cm chord. Thirteen transducers were installed on the airfoil to measure differential pressure and, hence, only normal force and moment coefficients are available. The data from the water tunnel tests were obtained on a model airfoil of four inches chord mounted in the water tunnel's 8.3- by 12-inch test section. The lift, drag, and moment were measured by an external balance with corrections for friction, but not for inertial loads, which were considered negligible (Ref. 19). The data from these two tests are compared with the Ames data in Fig. 18.

The CEAT data were obtained at three Mach numbers and show a Reynolds number about a third lower than the Ames tests. The Mach number for the water tunnel tests was, of course, zero and the Reynolds number varied from 100,000 to 250,000. This range of Mach and Reynolds numbers differs substantially from the Ames tests. The range of mean and alternating angles of attack for both the CEAT and water tunnel tests is comparable to the Ames test. Similarly, the range of reduced frequencies is also quite similar. For  $c_l$  as a function of minimum  $c_m$ , most of the test points for the CEAT and water tunnel tests are within the  $\pm 1\sigma$  bounds of the Ames test. At large  $c_m$  a few of the water tunnel results show higher lift values, while at  $c_m$  values nearer zero, both the CEAT and Ames water tunnel tests show some lift values that are low. No drag data are available from the CEAT test, but the Ames water tunnel data show good agreement with the Ames wind tunnel results, with only a few low points at the lowest drag values.

Because the CEAT test used differential pressure transducers, the integration of these pressures provides the normal force coefficient,  $c_n$ , rather than the lift coefficient,  $c_l$ . However, the differences between these two coefficients tend to be small and, within the approximate nature of the present analysis and the data scatter that is observed, it is appropriate to include  $c_n$  data when it is not possible to compute  $c_l$ . The difference between these two coefficients is illustrated in Fig. 19, which shows both coefficients for a dynamic stall loop for the NACA 0012 that was obtained during the Ames tests.

An extensive set of unsteady airloads and dynamic stall data have been obtained for the NLR-1 airfoil (Ref. 20, 21). The test data were obtained in the Boeing Supersonic Wind Tunnel, using a two-

dimensional subsonic insert. This tunnel is located in Seattle, WA. The airfoil chord was 6.38 in. and, with the installed subsonic insert, the test section was 36 in. high and 12 in. wide. Seventeen differential transducers were installed on the model and the pressures were integrated to provide  $c_n$  and  $c_m$ . The data were obtained over a Mach number range from 0.2 to 0.7 and for numerous combinations of mean and alternating angles of attack, both stalled and unstalled. For comparison with the Ames data, only test points with  $M = 0.2$  or  $0.3$  are used. In addition, test conditions have been excluded in those cases where the sum of the mean and alternating amplitude is less than the static stall angle of  $12.4^\circ$ .

Figure 20 compares the data from Ref. 20, 21 with the Ames tests. The Reynolds number in the Boeing tests is about 25% higher than the Ames tests. The range of mean and oscillating angles of attack is similar to the Ames tests with the unstalled cases removed. The range of reduced frequencies for the Boeing tests extend to 0.35, and this is beyond the range tested at Ames. The envelope of maximum  $c_n$  and minimum  $c_m$  for the Boeing test is similar to that obtained at Ames and the majority of test points fall within the  $\pm 1\sigma$  bounds of the Ames data. Note again, as in the case of the CEAT data for the VR-7 airfoil, these data are for the normal force coefficient rather than the lift coefficient.

## PARAMETRIC EFFECTS ON THE DYNAMIC STALL FUNCTION

Much of the focus of the two-dimensional dynamic stall testing over the last 35 years has been to understand the primary factors that influence dynamic stall and its prediction. Thus, investigators have looked at the influence of airfoil design, knowing that small changes in airfoil design strongly affect the character of static stall; that is, whether an airfoil shows leading-edge stall, trailing-edge stall, or a mixed stall. Just as important has been the effects of the angle of attack and its rate of change in the stall environment, and experimentalists have varied the mean angle of attack,  $\alpha_0$ , the alternating angle of attack,  $\alpha_1$ , and the reduced frequency,  $k$ , to provide an extensive range of parametric data to describe stall behavior. This is well illustrated for the Ames tests where the eight airfoils were tested over an extensive range of angles of attack and frequencies, as has been shown in Figs. 4 and 5. The dynamic stall function varies slightly, depending upon airfoil section used, but little effect of angle of attack and reduced frequency on the stall function is observed. This is not to suggest that these parameters are unimportant—the strength of the dynamic stall vortex depends directly upon these parameters. But, once stall

occurs, the relationship between maximum lift, maximum drag, and minimum moment is not influenced by these parameters.

The comparisons that have been shown for the VR-7 airfoil are surprising, perhaps, in that they indicate that Reynolds number does not appear to have a major effect on the dynamic stall function. Thus, data obtained from the Ames water tunnel for Reynolds numbers of 100,000 to 250,000, agree quite well with data measured in the wind tunnel with a Reynolds number of four million.

However, there are a number of parameters that may be important for characterization of the dynamic stall function and these have not yet been examined. These include (1) the boundary layer behavior, (2) variation in Mach number, (3) blade sweep effects, (4) three-dimensional effects (blade tip effects), and (5) the type of testing methods used to obtain the dynamic stall measurements. Four of these parametric effects will be discussed in following sections.

### Boundary Layer Transition Effects

Data were obtained in the Ames tests with a boundary layer trip to examine effects of boundary layer transition on dynamic stall. For some of the eight airfoils it appeared that the boundary layer trip influenced the dynamic stall function and, therefore, the tripped data were not used in deriving the polynomial fits in Tables 1 and 2. Figures 21 and 22 show the dynamic stall functions for the eight airfoils and compare the untripped and tripped data along with polynomial fits of these data. It appears that the effect of the boundary layer trip for the NACA 0012, AMES-01, and NLR-1 airfoils is to reduce the lift that is obtained in dynamic stall. However, for the FX 69-H-098, SC1095, and HH-02 airfoils the tripped behavior appears to be within the scatter of the untripped data. The VR-7 shows more scatter than the other helicopter sections and it is also unclear whether there is a clear difference between the tripped and untripped data. The NLR-7301 airfoil shows a greater reduction in the dynamic stall function because of the boundary layer trip than is observed for any of the helicopter sections.

It appears from the comparisons of the airfoil dynamic stall functions in Figs. 21 and 22 that boundary layer transition influences the stall on some of these airfoils. However, even when this effect is clearly measurable, the overall influence of transition characteristics is relatively small. The reasons why some of these airfoils show more sensitivity to the boundary layer transition than the other airfoils is not known.



## Mach Number Effects

Most of the Ames test data were obtained for  $M = 0.3$ , and it is not possible to determine the effects of higher Mach number on the dynamic stall function using these data. The dynamic stall data of Refs. 20 and 21 for the NLR-1 airfoil were obtained for Mach numbers from 0.2 to 0.7 and this range of Mach numbers makes this data set particularly useful. However, the NLR-1 dynamic stall characteristics differ somewhat from the other helicopter sections and these differences decrease the utility of this data set.

Figure 23 shows the maximum  $c_n$  as a function of the minimum  $c_m$  for six Mach numbers and a separate polynomial fit is used for each Mach number. As with the previous comparisons, data are only shown when the sum of the mean and oscillating angle of attack exceeds 12.4 deg. The dynamic stall functions appear similar for all of the Mach numbers tested. As Mach number increases, however, the extent of the augmented lift and negative pitching moment is reduced.

The polynomial fits from Fig. 23 are compared in Fig. 24. There is a general reduction in the dynamic stall function as Mach number increases, although this does not occur consistently at all pitching moments. The maximum change in the normal force coefficient as Mach number increases from  $M = 0.2$  to 0.7 is about  $-0.3$ .

In the previous examination of the Ames test data, it was shown that the  $a_0$  and  $b_0$  intercepts of the dynamic stall function were related to the measured values of static  $c_{l_{max}}$ . In general, static  $c_{l_{max}}$  decreases with increasing Mach number and it is of interest to determine if the approximate decrease in the  $a_0$  intercept observed in Fig. 24, is similar to changes in the static  $c_{l_{max}}$  characteristics. Figure 25 compares the measured  $c_{n_{max}}$  from Ref. 20 with a best estimate of the intercepts of the polynomials shown in Fig. 24. The dynamic stall function  $a_0$  intercepts were estimated from Fig. 23, by using the polynomials for  $M = 0.2$  and 0.3 and then adjusting this curve to best match the data in the figure. The computed polynomial intercepts at the higher Mach numbers were not used, as these polynomials show excessive curvature. The comparison shown in Fig. 25 indicates that the  $c_{n_{max}}$  and the best estimate of the intercept show a similar trend, but the intercept estimate is less affected by Mach number variation than the measured  $c_{n_{max}}$ .

The estimated intercepts from Fig. 25 can be used to "correct" the  $c_n$  and  $c_m$  data by adjusting the steady part of the data so that they are referenced to one Mach number, that is,

$$\hat{c}_n = c_n - \Delta c_n \quad (10)$$

where

$$\Delta c_n = \bar{c}_n(M) - \bar{c}_n(0.3) \quad (11)$$

The  $\hat{c}_n$  is the corrected normal force coefficient,  $\bar{c}_n(M)$  is the static  $c_{n_{max}}$  obtained from the best estimate in Fig. 25, and  $\bar{c}_n(0.3)$  is the static  $c_{n_{max}}$  at  $M = 0.3$ . Figure 26 shows all of the dynamic stall data for the NLR-1 airfoil with and without these corrections. Without corrections the polynomial fit shown here provides a good fit of the data with an  $r^2$  value of 0.82. The corrections to the data do not improve the fit, and the  $r^2$  value shows a slight decline.

The examination of Mach number effects shown here suggests that there is a small influence of Mach number on the dynamic stall function, but that within the constraints of experimentally observed data scatter it may not be possible to obtain corrections for these effects.

## Effects of Blade Sweep

Unswep data for an NACA 0012 airfoil section from Ref. 16 were compared with the Ames test data in a previous section. This data set is also useful in that it allows the direct comparison of swept and unswept test data for dynamic stall. These data were obtained in Ref. 16 for two sweep angles, 0 deg (unswept) and 30 deg. The onset Mach number,  $M_\infty$ , was varied depending upon sweep angle so that the Mach number normal to the leading edge,  $M_c$  was the same for all sweep conditions, that is,

$$M_c = M_\infty \cos \Lambda \quad (12)$$

where  $\Lambda$  is the sweep angle. The reduced frequency was also selected based on the chordwise Mach number. The pressure transducers were mounted in a chordwise array, rather than a streamwise array for the swept conditions, and the dimensional forces and moment were obtained for this chordwise array. However, the coefficient forces and moments were then calculated with the sweep effects included, that is,

$$\begin{aligned} c_n(t) &= N(t) / c q \cos^2 \Lambda \\ c_m(t) &= M(t) / c^2 q \cos^2 \Lambda \\ c_c(t) &= C(t) / c q \cos^2 \Lambda \end{aligned} \quad (13)$$

The final  $c_l$  and  $c_d$  coefficients were then resolved using eq (5).

The dynamic stall functions of the NACA 0012 airfoil are compared for sweep angles of 0 and 30 deg. in Fig. 27. The data include not only the unswept data

shown previously in Fig. 16, but also data obtained at a chordwise Mach number of 0.4 for both sweep angles. Polynomials have been fitted to both swept and unswept data to assist the comparison. The two sets of data appear to be in good agreement over the mid-range of  $c_m$  and  $c_d$  values. However, at moment coefficients greater than  $-0.35$  or  $-0.40$ , the swept data show less lift, while at the moments less than  $-0.10$ , the swept data appear to have slightly greater lift.

### Comparison of Oscillating and Ramp Tests

Dynamic stall data were obtained for the Sikorsky SSC-A09 airfoil in the UTRC Large Subsonic Wind Tunnel using two modes of dynamic stall testing (Ref. 22). The first mode of testing was to oscillate the airfoil around a mean angle of attack in the same manner that was used in the Ames tests. In the second mode the airfoil angle of attack was increased at a linear rate, that is, a ramp function was used.

The SSC-A09 airfoil is a nine percent thick airfoil with a relatively sharp leading edge radius. It was designed to maintain the performance characteristics of Sikorsky's second-generation airfoils, such as the SC1095, at lower Mach number but to increase the drag divergence Mach number at zero lift (Ref. 23). In this sense the SSC-A09 may be considered a third-generation airfoil.

The model chord was 17.3 in. with 18 pressure transducers installed on each surface. The pressures on the airfoil were integrated to obtain the  $c_n$ ,  $c_c$ , and  $c_m$  coefficients and these were converted to the  $c_l$  and  $c_d$  coefficients in the wind tunnel axes using eq (5).

The measured extrema for lift, moment, and drag are shown in Fig. 28 for both modes of testing. Although the quantity of data are limited, particularly for the oscillating tests, polynomial fits have been added to the curves to better illustrate the differences. The basic character of the dynamic stall function observed previously for the second-generation airfoils is similar to that of this airfoil. The ramp tests appear to show a slightly greater lift augmentation during dynamic stall than is seen for the oscillating tests, although this is less apparent for the lift-drag "polar" than for the maximum lift as a function of minimum moment.

The SSC-A09, although a third-generation airfoil, does not appear to be as good in dynamic stall as the SC1095. Figure 29 compares the dynamic stall characteristics of this airfoil from the oscillating airfoil testing with the polynomial that was derived from the Ames SC1095 test data. Although the number of test

points are limited, it appears that the SSC-A09 shows 0.1 to 0.3 less augmented lift than the SC1095 for the same moment or drag conditions. This airfoil was optimized for improved transonic performance (Ref. 23) and this appears to have resulted in some additional penalty in moment and drag under maneuver conditions.

### COMPARISON WITH FLIGHT TEST DATA

Reference 12 has examined dynamic stall on a highly-instrumented UH-60A helicopter for three conditions: a level flight case at high altitude, a diving turn at high load factor, and the UTTAS pull-up maneuver. This examination has demonstrated that dynamic stall is remarkably similar for all of these flight conditions and, in general, can be characterized by the shedding of a vortex from near the leading edge of the blade, just as has been observed in two-dimensional wind tunnel testing. It is of considerable interest, therefore, to see if this good qualitative agreement extends to the dynamic stall function that has been defined here for the two-dimensional test data.

The UTTAS pull-up maneuver from Ref. 12 (Counter 11029) has been re-examined to obtain maximum  $c_n$  and  $c_m$  values from the flight data that correspond with the extrema obtained from the two-dimensional tests. The maneuver examined is basically a symmetric pull-up that has been modified so that the entry is made from level flight at  $V_H$ . For the case here, Counter 11029, a load factor of 2.1g was obtained during the pull-up. The measured oscillatory pitch-link loads in this maneuver are shown in Fig. 30. In this figure each symbol represents one revolution of the rotor. At the maneuver entry point, the oscillatory loads are just under 1000 lb and, then, at about Rev 09, the loads rapidly increase until they reach a plateau at about Rev 14. These loads are maintained through Rev 22 for a duration of a little over two seconds and then rapidly return to level flight values. This maneuver is particularly useful for comparison purposes as there are generally one to three cycles of stall during each revolution from Rev 08 to Rev 25 and this provides many  $c_n$ - $c_m$  pairs.

A second reason for the selection of the UTTAS pull-up is that the maneuver is representative of the load limits for this aircraft. The peak oscillatory pitch-link load measured during this maneuver is about 2860 lb. The largest pitch-link loads that were obtained during air-to-air combat testing on this aircraft were 2700 lbs and the maximum loads encountered in the original flight loads survey were 3040 lbs (Ref. 24).

An example of the integrated  $c_n$  and  $c_m$  coefficients on the outer portion of the blade is shown in Fig. 31. The data here extend from 0 deg to 360 deg and, based on the nomenclature of Ref. 12, include the final 135 deg of Rev 13 and the first 225 deg of Rev 14. Under unstalled conditions the  $c_n$  can achieve relatively high levels, but the  $c_m$  are smooth and are seldom less than about  $-0.10$ . The rapid variation seen in  $c_m$  in Fig. 31 is the best indicator of the shedding of a dynamic stall vortex. For each potential stall event the lift and moment time histories, as shown in Fig. 31, were examined. If extrema in lift and moment showed behavior typical of the shedding of a dynamic stall vortex, that is, the moment minimum lagged the lift maximum, then both the peak  $c_n$  and  $c_m$  coefficients were recorded as well as the associated azimuth angles. The mean azimuth angle for a dynamic stall point was used to compute the Mach and Reynolds number based on the local velocity, that is,

$$V(r, \psi) = V_T \left( \frac{r}{R} + \mu \sin \psi \right) \quad (14)$$

The reduced frequency was approximated depending upon whether the stall cycle was the first, second, or third. Referring to the sketch in Fig. 32, based on Rev 14, each symbol represents the azimuth that is associated with a stall event. The azimuthal spacing between stall cycles is defined as  $\Delta\psi_{12}$  and  $\Delta\psi_{23}$ . The oscillation frequency associated with each cycle, is approximated

$$\begin{aligned} \omega_1 &\approx (360 / \Delta\psi_{12}) \\ \omega_2 &\approx 0.5[(360 / \Delta\psi_{12}) + (360 / \Delta\psi_{23})] \\ \omega_3 &\approx (360 / \Delta\psi_{23}) \end{aligned} \quad (15)$$

and the reduced frequency is

$$k = \frac{\omega_i \Omega c}{2V(r, \psi)} \quad (16)$$

The frequencies associated with these stall cycles are a consequence of the control system flexibility. Measurements made of the control system stiffness for this aircraft, Ref. 25, indicate that this frequency is about 4.2/rev. If the reduced frequency was defined based on the fundamental rotor frequency, that is, 1/rev, then the computed values would be a quarter of those that are computed using eq (15).

Figure 33 compares the flight test data with the Ames test data for the SC1095 airfoil. The  $c_n$  and  $c_m$  coefficients for each stall event are categorized as either the first, second, or third stall cycle, and different symbols are used in Fig. 33 to indicate the cycle. The Reynolds and Mach numbers are generally larger than those recorded in the Ames tests, as expected for a full-scale flight vehicle. The first cycle, which occurs on the retreating side of the

disk, occurs at a low Mach number and a number of these cases overlap the Ames test data. The second cycle occurs at moderate Mach number, while the third cycle stall events occur at quite high Mach numbers. The reduced frequencies in flight, based on eq (15), are considerably higher than those used in the wind tunnel tests. However, a good argument can be made that the reduced frequency should be based on the rotor fundamental frequency at 1/rev, particularly for the first cycle. If this change is made, the reduced frequencies in Fig. 33 are reduced by roughly a factor of 4. The general hyperbolic character of the reduced frequency with Mach number is the effect of the local velocity term in the denominator of the reduced frequency, see eq (16). The highest reduced frequencies are associated with the lowest velocities, for instance, for Cycle 1 at the more inboard radial stations.

The plot of the maximum normal force coefficient as a function of the minimum moment coefficient in Fig. 33 shows that the dynamic stall loading in flight is roughly similar to the wind tunnel tests, but the values of lift are less for moments approaching zero, and higher for the deep dynamic stall conditions. Moreover, the flight data exhibit considerable scatter in comparison to the wind tunnel tests.

The flight data shown in Fig. 33 are for a full range of Mach numbers and, based on the previous examination of the NLR-1 data, it is expected that the Mach number will affect the dynamic stall function although it is not clear how to best correct for this effect. The data shown in Fig. 33 are for not only the SC1095 airfoil (0.865R, 0.92R, 0.965R, and 0.99R) but also for the SC1094 R8 airfoil (0.675R and 0.775R). An attempt to "correct" these data has been made by using the variation of static  $c_{l_{max}}$  with Mach number obtained from Ref. 1. The SC1095 data have been corrected to  $M = 0.3$  using that airfoil's  $c_{l_{max}}$  variation and the SC1094 R8 data have corrected to the same Mach number using that airfoil's  $c_{l_{max}}$  variation. The corrected data are compared to the Fig. 33 data in Fig. 34. A polynomial fit of both the uncorrected and corrected data is shown in Fig. 34 along with the polynomial fit for the SC1095 airfoil from Table 1 (based on  $c_p$ , not  $c_n$ ). No improvement is seen in the coefficient of determination,  $r^2$ , for the corrected data, but there is a reduction in the standard deviation of 19%. The standard deviation for the flight data, about 0.25, is still much greater than observed for the SC1095 airfoil tested in the wind tunnel, where a value of 0.07 was obtained; see Table 1.

## DESIGN CONSIDERATIONS

Test data on airfoils oscillating in pitch show that the airfoil's lift is augmented dynamically beyond the static stall angle although this additional lift is accompanied by penalties in pitching moment and drag. This is illustrated in Fig. 35 where the maximum lift and drag, and minimum moment for the SC1095 airfoil obtained from the Ames tests are shown. The dashed lines represent the polynomial fits from Tables 1 and 2 for this airfoil. Steady section data for the SC1095 are also shown in this figure and the difference between the steady lift and the dynamic stall function is an indication of the augmented lift that is possible because of dynamic stall. The steady section data were obtained at low speed in the Glenn L. Martin Wind Tunnel at the University of Maryland in the tests reported in Ref. 26 and are shown for angles of attack from zero to 55 deg.

Crude boundaries have been added to Fig. 35 to indicate limits on airfoil section moment and drag based on pragmatic considerations. In the case of the section pitching moments, variation at 1/rev or higher frequencies will cause oscillating loads in both the rotating- and fixed-control systems that will cause fatigue damage if they are excessive. Torsional loading typically increases with forward speed and is greatest at the maximum forward flight speed (Ref. 27). These torsion moments are largely caused by unsteady aerodynamic loads that are not related to blade stall. An examination of flight test data from the UH-60A (Ref. 28) shows that the minimum section moment recorded at the maximum level flight speed is about  $-0.15$ , and that value has been used as the bound in Fig. 35. Although there are numerous factors that affect rotating and nonrotating system component endurance limits, to a first approximation this boundary represents operation that can be safely performed without encountering fatigue damage.

The boundary for the section drag in Fig. 35 is based on the ability of a helicopter to continuously maneuver using available engine power, without having to convert forward speed or altitude into power. In estimating this boundary it is assumed that a helicopter is maneuvering near its minimum power speed where the greatest amount of excess power is available. The profile power in this situation (Ref. 29) is

$$C_{P_0} = \frac{\sigma c_{d_0}}{8} (1 + 4.6\mu^2) \quad (17)$$

It is assumed that induced and parasite power change only slightly in a maneuver and that the excess power available is used by the profile power. For these conditions the power available is roughly twice the power required in level flight or four times the profile power. For the

UH-60A in level flight, a nominal  $c_{d_0}$  is about 0.0085. If all the excess power is made equivalent to the  $c_{d_0}$  term, then this is equivalent to a profile drag of about 0.034. However, the blade is not stalled over the entire disk, so the estimated boundary is set at roughly three times this value or a  $c_{d_0}$  of roughly 0.1. The estimate of this boundary is quite crude, but it does give a rough idea of airfoil conditions where a helicopter can maneuver without having to descend to maintain power to the rotor. At higher speeds, the helicopter has the option to bleed off airspeed to provide power to the rotor when there is dynamic stall on the disk. In severe maneuvers a helicopter will always require additional power to maintain thrust, either by reducing airspeed or by descending.

### Preliminary Design

Military and civilian designs differ in their need for maneuver capability. A civilian helicopter does not require that rotating and fixed-system controls be designed for substantially more section moment capability than is shown by the boundary in Fig. 35. A military helicopter will, on occasion, require substantially more maneuver capability than a civilian aircraft. The data from the UH-60A shown in Fig. 34 show lift coefficients as high as 3.5 with an associated section moment of  $-0.7$ . However, this sort of maneuver requirement represents a very small fraction of the military aircraft's usage spectrum. Civilian aircraft, although not requiring this kind of maneuver capability, do need the ability to safely encounter the loading that occurs in inadvertent maneuvers, obstacle avoidance, or similar severe, but infrequent conditions.

The prediction of the control loads caused by dynamic stall in maneuvers is currently beyond the state of the art. Thus, in a new design, or a modified aircraft, it is necessary to scale the loads from previous flight test data. However, in doing this scaling there are both aerodynamic or performance aspects as well as structural aspects that need to be taken into account. As an example, consider the upgrade of an aircraft where the gross weight is increased by 30% yet the aircraft is to retain the same maneuver capability. For a limiting maneuver,  $C_T^*/\sigma$ , there is an associated limiting airfoil section lift,  $c_l^*$ , and moment,  $c_m^*$ . As

$$\frac{C_T^*}{\sigma} = \frac{T}{\rho b c R V_T^2} \quad (18)$$

then if the thrust,  $T$ , is increased by 1.3, then either  $b$ ,  $c$ , or  $R$  (or some combination) must also be increased by a factor of 1.3. If the blade number,  $b$ , is increased from 4 to 5, then it is possible to avoid major changes in chord

or radius. Alternatively, the blade number and radius may be held constant and the chord (and solidity) increased instead. The dimensional aerodynamic moment on the blade is

$$M_a = \frac{1}{2} \rho c V(r, \psi)^2 c_m^* \quad (19)$$

This moment is unchanged if the additional thrust is obtained by increasing blade number and thus the rotating controls loads will not be affected. However, if the chord is increased by 1.3, then the aerodynamic moment will also be increased by 1.3 and the rotating controls will have to be resized.

The nonrotating control system is not dependent upon the choice of  $b$  or  $c$  for obtaining the increased rotor thrust. As an example the moment about the fixed-system swashplate is

$$M_{sp} \propto b r_{sp} M_a \quad (20)$$

Thus, if the chord is increased the blade aerodynamic moment will increase, while if blade number is increased, the aerodynamic moment will stay the same but the fixed-system controls will see the same increase.

### Stall Prediction with Semi-empirical Models

Most comprehensive analyses now in use in the helicopter industry, government agencies, and academia use some form of lifting-line theory to calculate the aerodynamic loads on the rotor. In these analyses the steady aerodynamic forces and moment are based on tables or formulae from two-dimensional wind tunnel tests. The steady data are then modified to account for unsteady aerodynamics in the calculation of the loading. For angles of attack beyond the static stall angle, this approach underpredicts the aerodynamic loads and some form of semi-empirical dynamic stall model is used to provide the lift, drag, and moment as a function of angle of attack. The dynamic stall function that has been introduced in this report provides a first check of these semi-empirical models.

Gangwani (Ref. 17) has described a semi-empirical stall model with multiple parameters that are identified by fitting a select number of dynamic stall loops from two-dimensional wind tunnel tests. In Ref. 17, results are presented for both the NACA 0012 and SC1095 airfoils. The predicted lift and moment extrema using Gangwani's model are compared with the data in Fig. 36. It is unclear in Ref. 17 whether all of the data used for the comparisons were also used in the fitting process. Regardless, good agreement is observed between the synthesized data and measurements for blade loading.

A workshop on dynamic stall was held at NASA-Ames Research Center in 1992 to compare the predictions of dynamic stall models with test data (Ref. 30). For this purpose, data from tests on an oscillating wing with an NACA 0015 profile were used as a baseline (Ref. 31). The experimental test point selected for the calculations was a 3-D case with the measurements obtained at the 47.5% span location of the wing. However, comparison of the data at this span with two-dimensional test data obtained during the same program shows that the maximum lift and drag, and minimum moment are only slightly affected by three-dimensional effects at this inboard location. This case is interesting in that it represents a "blind" test in that the collaborators who made the calculations did not have access to these data until the workshop.

The semi-empirical models used for the workshop calculations included the Beddoes and Leishman indicial models, a model for three-dimensional stall from ONERA, a version of the Boeing stall model, and the 2GCHAS model. The Beddoes indicial model is an evolution from an earlier indicial model (Ref. 32) and includes three-dimensional effects (Refs. 33, 34). The Leishman indicial model also derives from Ref. 32, but was developed for Sikorsky Aircraft and is proprietary. The ONERA model is based on potential flow theory and is described in Ref. 35. It is not related to the well known ONERA dynamic stall models developed by Tran and Petot (Ref. 36). The 2GCHAS dynamic stall model is also derived from Ref. 32 and was developed by Leishman. Finally, the Johnson model is an implementation of the Boeing dynamic stall model (Ref. 37) in the CAMRAD II comprehensive analysis.

The data and the five semi-empirical models for the workshop condition are compared in Fig. 37. It is noted that the reference data point for the NACA 0015 test is below the NACA 0012 fit based on the earlier Ames tests. The predictions of most of the semi-empirical models in Fig. 37 show good agreement with the lift, but underpredict the moment and drag. Only the 2GCHAS model provides a reasonably accurate prediction of each of the three coefficients.

Currently, the comprehensive analysis CAMRAD II includes five semi-empirical dynamic stall models (Ref. 38). These include two of the older, simpler models used by Boeing (Ref. 37) and Johnson (Ref. 39), the Leishman-Beddoes model (Ref. 30), and two ONERA models: the Edlin method developed by Tran and Petot (Ref. 36), and Truong's Hopf Bifurcation model (Ref. 40). As each of the models is semi-empirical it is necessary to adjust or identify the model parameters based on test data. This has been done within CAMRAD II for the NACA

0012 airfoil, but not for other airfoils. Thus, it is expected that these models will provide a better prediction of the NACA 0012 characteristics than for other sections.

The predictions of the five models are compared with single test points for the NACA 0012 and SC1095 sections in Fig. 38. The selected test points represent moderate to fairly severe stalled conditions. Most of the models provide a reasonable prediction of the maximum lift, but are substantially less accurate in predicting the minimum moment. In particular, the Boeing and ONERA Edlin models show a significant underprediction of the negative moment. The other models show poor-to-fair agreement in moment. Although it was anticipated that the predictions for the NACA 0012 would be better than for the SC1095, since the semi-empirical parameters in the models are based on NACA 0012 test data, this is not the case.

The three examples of predictions of the semi-empirical models shown here provide mixed results. Gangwani's method is compared with the data over a range of vortex strengths and shows good results. The other methods, however, are evaluated for only one loading condition and it is more difficult to judge them. In the case of the NACA 0015 data, the 2GCHAS model provides a good calculation for this single case, while the other methods are less accurate. The wide variation in the moment predictions that is observed here will likely result in an inaccurate calculation of the torsional deformation of the blade and the related angles of attack. Except for Gangwani's model, no suitable calculation of the loads in stalled flight can be expected from these methods.

### Stall Prediction By Direct Calculation

Numerous numerical methods have been developed for the direct calculation of dynamic stall on an oscillating airfoil and this approach remains an exciting challenge for investigators interested in classical fluid mechanics. These methods, presently, are at a research or pilot stage and there has been no anticipation of their use within the design process. Eventually, however, it is envisioned that the best of these methods will show some utility in the development of semi-empirical models used within the comprehensive analyses, much as current steady two-dimensional Navier-Stokes flow solvers are used to develop coefficient tables for these analyses (Ref. 41).

One approach to direct calculation is to solve the incompressible, unsteady, two-dimensional viscous flow equations using vorticity as the primary variable and solving the equations following a conformal mapping of the physical domain to a circular region (Ref. 42). The

code used in this approach is called the ZETA code. Calculations have been made using the ZETA code for both the VR-7 airfoil (Ref. 43) and the VR-12 airfoil (Ref. 44). The VR-12 airfoil, Fig. 39, is thinner than the VR-7 and is designed for better performance at high Mach numbers. Dynamic stall data for the VR-7 airfoil have been discussed previously, including data from water tunnel tests at NASA-Ames Research Center (Ref. 19). The same facility has also been used to obtain dynamic stall data on the VR-12 (Ref. 44). Figure 40 compares the experimental measurements for these two airfoils with the predictions for one condition using the ZETA code. The single experimental case that is computed by the ZETA code is indicated by the solid circles. The VR-7 polynomials from Tables 1 and 2 are used as a reference for the VR-12 data and show fairly good agreement.

The reference test conditions in Fig. 40 represent a moderate to severe dynamic stall case. For the VR-7, the ZETA code overpredicts the moment and drag (slightly), and significantly underpredicts the lift, missing the experimental value by  $\Delta c_l = -0.3$ . For the VR-12, the ZETA prediction falls directly on the VR-7 dynamic stall function, but the dynamic stall vortex strength is clearly too strong and lift, drag, and moment are significantly overpredicted.

The AFDD workshop, mentioned previously, included a blind comparison of semi-empirical models with a test condition from an oscillating wing dynamic stall test. This blind comparison also included calculations using two Navier-Stokes flow solvers. The first solver, Srinivasan's TURNS code (Ref. 45), solves the Reynolds averaged thin-layer Navier-Stokes equations and uses the Baldwin-Lomax turbulence model. The second solver (Ref. 46) has been developed at the Georgia Institute of Technology (GIT) by Prof. Sankar and his students. The predictions of these two codes are compared with the light or moderate stall condition from the NACA 0015 experiment in Fig. 41. Both codes provide a good prediction of the lift, but the moment and drag predictions are unsatisfactory. The TURNS code shows little or no effect of the stall cycle on moment and drag, while the Georgia Tech code significantly overpredicts both moment and drag. The comparison here is for the extreme values only. An examination of the original comparison (Ref. 30) shows large errors in the phase of the loading in the Georgia Tech code.

Rouzaud and Plop have reported the development of a Reynolds-averaged, Navier-Stokes solver at ONERA (Ref. 47). They have examined the effects of two turbulence models; those of Baldwin and Lomax, and Launder and Sharma. They have compared their analysis with a severe stall case for the NACA 0012 from the

Ames tests. These predictions, along with the Ames test data, the reference point, and the polynomial fits from Tables 1 and 2, are compared in Fig. 42. The calculations with the Baldwin-Lomax model severely overpredict the moment, and the drag is also high. However, the prediction using the Launder-Sharma model provides good results. In this sense, the Launder-Sharma model passes the necessary condition that there must be a good prediction of the extrema. However, an examination of the time behavior of the coefficients in Ref. 47 shows that the extrema occur over a very short range of time steps compared to the data and there is an associated phase shift. In addition, the experimental case used here included two shed vortices (Ref. 10) and the Navier-Stokes calculations indicate only a single vortex.

The direct calculation results shown here are quite mixed and, in general, are not accurate. The ONERA results, in particular, indicate that the calculations are sensitive to the turbulence modeling and this obviously represents a serious challenge for these computations. The great expense of these computations, unfortunately, works against extensive testing of these methods. As a minimum, however, it appears necessary that these methods should be compared to at least each of the dynamic stall cases from the Ames experiments that have been shown to be qualitatively different, that is, stall cases without a clear shed vortex, cases with a single vortex, and cases with two vortices.

## MULTI-ELEMENT AND NONCONVENTIONAL AIRFOILS

As has been shown here, conventional, single-element airfoils show similar dynamic stall characteristics. Although it is expected that small gains in performance, in terms of dynamic stall, may be obtained through careful design, substantial improvements do not appear feasible. It may be possible, however, to enhance dynamic stall performance using multi-element or variable geometry airfoil designs. Two multi-element airfoils and an airfoil that represents the limiting condition of a variable-geometry airfoil have been investigated in the Ames water tunnel (Refs. 19, 44, and 48). In addition, ZETA code calculations have been made for these configurations as well as for an airfoil with blowing on the upper surface (Ref. 43, 44). These measurements and calculations are examined here.

A VR-7 airfoil has been tested in the Ames water tunnel in both a baseline configuration and a configuration with a leading edge slat. Data were obtained over a range of reduced frequencies and Reynolds number for a case with a mean angle of attack of 15 deg and an

alternating angle of 10 deg (Ref. 19). A single test point from this data set has also been used as a basis for calculations using the ZETA code. The airfoil and slat are shown in Figure 43 along with comparisons of the experimental data and the calculations. For these tests the main airfoil is the VR-7 and it is identical to the airfoil tested in the Ames wind tunnel tests. The baseline VR-7 and the main element shown in Fig. 43 are identical. The slat is placed forward of the main airfoil and slightly below the mean chord line.

The baseline VR-7 data show good agreement with the VR-7 dynamic stall function and this was discussed previously, see Fig. 18. The data measured for the configuration with the slat show a substantial increase in lift and, perhaps more important, a significantly reduced penalty in terms of moment and drag. Two reference points were selected for these two configurations and the ZETA code was used to calculate the airfoil loading. For the baseline airfoil the lift is underpredicted and the moment overpredicted, as noted before in the discussion of the ZETA code predictions; see Fig. 40. The prediction for the slat configuration is substantially worse, with the lift significantly underpredicted and the moment and drag overpredicted. The calculations, in this case, do not show the same improvement in dynamic stall performance as shown by the data.

A similar test was performed on a baseline VR-12 airfoil and a multi-element configuration (Ref. 44) and calculations were again made with the ZETA code (Ref. 43, 44). In this case, however, rather than adding a leading edge slat to the airfoil, an extendable leading edge was designed, that when retracted, would fit inside the profile of the unmodified VR-12. The VR-12 with the extended leading edge, the experimental data, and the calculations are shown in Fig. 44. As the VR-12 was not one of the original eight airfoils tested in Ref. 9, there is no polynomial fit based on experimental data, so the VR-7 fit has been used instead. The data from the baseline VR-12, as well as the modified airfoil, show good agreement with the VR-7 polynomials. Unlike the VR-7 configuration with a slat, however, no improvement in dynamic stall performance is observed for this airfoil with an extended leading edge. The ZETA calculations in this case quite closely match the VR-7 dynamic stall function, but the lift and moment are substantially overpredicted for both airfoils, and the drag is overpredicted for the baseline airfoil.

The ZETA code has been used in Ref. 43 to examine the potential of variable-geometry airfoil configurations to provide augmented lift for maneuverability, without the associated penalties in moment and drag. Calculations were made for a VR-12

airfoil that was modified by rotating the first 25% of the airfoil about the quarter chord point. Two configurations were examined. In the first configuration, Case 2513, the forward portion of the airfoil was rotated 13 deg nose down and fixed at this location. In the second configuration, the forward portion was moveable. In Ref. 43 this configuration was referred to as the variable-droop leading-edge (VDLE) airfoil. Under normal circumstances, the forward portion was fixed at zero deg, but when the angle of attack exceeded 13 deg, the forward portion rotated nose down proportional to angle of attack,

$$\theta = \alpha - 13 \quad (21)$$

where  $\theta$  is the droop or rotation angle of the forward portion. No experimental validation of the variable-geometry configuration has yet been obtained, but Case 2513, with the nose rotated down by 13 deg has been evaluated in the Ames water tunnel (Ref. 48). The experimental stall characteristics of the deformed airfoil are compared with an unmodified VR-12 in Fig. 45. For identical mean and alternating test conditions, there is a general reduction in the strength of the dynamic stall vortex for the Case 2513 tests, but this configuration shows the same dynamic stall function as seen for the unmodified airfoil. Thus, for the test conditions examined, the Case 2513 airfoil provides no benefit. The ZETA code was used to calculate a single test point to compare with the experimental data. For the calculation the lift is underpredicted, as are the moment and drag. However, the calculated values agree well with the VR-7 polynomial fit.

The ZETA code was also used in Ref. 39 to examine the effect of upper surface blowing on dynamic stall performance. This was done by changing the normal no-slip flow condition for a number of grid points on the airfoil upper surface near the quarter chord. The normal no-slip condition is referred to here as the zero blowing case, and a boundary condition with the velocity set to twice the free stream is called 2X blowing, and so forth. The results of these calculations are shown in Fig. 46. As these calculations were made for an NACA 0012 airfoil, the polynomial for this airfoil is used as a reference line. In the case of zero blowing the ZETA code shows the presence of a dynamic stall vortex, although the lift is underpredicted. With blowing, the dynamic stall vortex is eliminated and there is no lift augmentation for this condition. The suppression of the dynamic stall vortex in this case offers no advantage to the designer seeking improved maneuverability characteristics.

## CONCLUSIONS

The loading in lift, moment, and drag has been examined for eight airfoils tested in the NASA-Ames 7-by 10-Foot Wind Tunnel for an extensive range of test conditions that result in the shedding of one or more dynamic stall vortices from the leading edge of the airfoil. The loading studied here is represented by the peak lift, moment, and drag during a dynamic stall loop, as these are the parameters that are related to maneuver limits for helicopters in flight. That is, the peak lift coefficient is related to the available thrust, the peak moment is related to control system loads, and the peak drag is related to power requirements. Based on this evaluation, the following conclusions are made:

1. Each airfoil shows a characteristic relationship between the peak lift, peak moment, and peak drag over all test conditions for a wide range of airfoil operating conditions. This characteristic, herein referred to as the dynamic stall function, is a clear indication of the importance of the loading caused by the dynamic stall vortex as it forms on the airfoil, convects along the upper surface, and finally leaves the airfoil at its trailing edge.
2. The dynamic stall functions of the eight airfoils are remarkably similar. However, the one fixed-wing section included in the comparison, the NLR-7301, shows somewhat different characteristics.
3. Polynomials fitted to the test data allow the estimate of the lift coefficient for zero moment and zero drag conditions, that is the intercept of the polynomial ( $a_0$ ,  $b_0$ ). In general, the intercept values are observed to be 0.1 to 0.2 higher than the static  $c_{l_{max}}$ .
4. The polynomial intercepts,  $a_0$  and  $b_0$ , provide a rough approximation of an airfoil's dynamic stall performance, that is, how much lift an airfoil can produce at a fixed penalty in moment and drag. These intercepts appear proportional to the static  $c_{l_{max}}$  and, therefore, an airfoil with an improved  $c_{l_{max}}$  can reasonably be expected to have improved dynamic stall performance.

Data obtained from five independent tests of four of the eight airfoils in the Ames test series have been compared to the Ames data and it is concluded that the dynamic stall function of an airfoil is the same regardless of the test facility or testing rig used. This includes tests obtained in both wind tunnels and a water tunnel.



A number of parametric effects on the dynamic stall function have been examined using either the Ames test data or other data sets. It is concluded that

1. The amplitude and the frequency of the airfoil oscillation do not influence the dynamic stall function although they strongly effect the strength of the dynamic stall vortex.
2. Reynolds number does not affect the dynamic stall function.
3. Boundary layer behavior, as controlled by a trip on the airfoil surface, has a small effect on the dynamic stall function for some airfoils, but not for others. For those airfoils influenced by a boundary layer trip, the stall performance is reduced, that is, the lift is reduced for a fixed moment or drag condition.
4. Mach number has a small but important effect on the dynamic stall function. It appears that the shape of the function is unchanged, but the intercept of the dynamic stall function is reduced with Mach number in a fashion similar to the reduction that is observed in static  $c_{l_{max}}$ .
5. The sweep angle does not show a clear effect on the dynamic stall function although a greater range of test conditions is probably required to confirm this conclusion.

Flight test data obtained on a UH-60A helicopter in a limiting maneuver show a dynamic stall function similar to that observed in two-dimensional wind tunnel tests, although the scatter in the data is increased.

The problem of design for improved maneuverability for a helicopter has been examined and it is concluded that

1. Conventional airfoil design presently offers little opportunity for increased helicopter maneuverability. However, specific characteristics that provide improved performance in unstalled flight may be detrimental for stall performance.
2. If increased maneuverability is required for a helicopter, then it is necessary to increase rotor solidity. However, increases in rotor solidity will also increase the loads in the rotating- or fixed-system controls or both.
3. Based on the examination of the predictive capability of a number of the semi-empirical models for dynamic stall that are currently in use, it appears that it is sometimes possible to obtain good results. However, in the majority of cases, the present

methods show a wide variation in the predicted loading and do not appear to be suitable for design.

4. An examination of a limited set of aerodynamic load calculations using two-dimensional Navier-Stokes flow solvers suggests that substantially more progress is required for this difficult problem before these methods can usefully support design.

Limited experimental and analytical efforts looking at multi-element or variable-geometry airfoils were examined in the context of the dynamic stall function. Based on experiment, it appears that multi-element airfoils may provide increased lift in some cases without a severe moment or drag penalty, but this is not obtained for all configurations. However, the calculations used in these cases do not provide useful information concerning the dynamic stall loading.

The dynamic stall function introduced in the present study provides a useful means of evaluating the accuracy of calculations for dynamic stall, and a means of assessing experimental measurements of new or novel airfoil sections.

## ACKNOWLEDGMENTS

Leo Dadone of Boeing Helicopters in Philadelphia is acknowledged for his discussion of the helicopters sections used on aircraft made by Boeing. Robert Flemming of Sikorsky Aircraft is acknowledged for his comments on Sikorsky Aircraft airfoils and testing. Frank Harris is acknowledged for his useful comments on this manuscript. Prof. Gordon Leishman of the University of Maryland is acknowledged for supplying steady test data from the wind tunnel tests of the SC1095 and SC1094 R8 airfoils reported in Ref. 26. Jim Narramore of Bell Helicopter Textron is acknowledged for his discussion of the use of airfoil sections on aircraft manufactured by Bell Helicopter. Roger Smith of Boeing Helicopters in Mesa is acknowledged for his discussion on the Apache rotor design and his useful comments on this manuscript.

## REFERENCES

1. Joseph Totah, "A Critical Assessment of the UH-60 Main Rotor Blade Airfoil Data," 11th AIAA Applied Aerodynamics Conference, Monterey, CA, August 9-11, 1993.

2. Franklin D. Harris, "Rotary Wing Aerodynamics—Historical Perspective and Important Issues," American Helicopter Society National Specialists' Meeting on Aerodynamics and Aeroacoustics, Arlington, TX, February 29-27, 1987.
3. Frank J. McHugh, "What Are the Lift and Propulsive Force Limits at High Speed for the Conventional Rotor?" American Helicopter Society 34th Annual National Forum, Washington, D.C., May 15-17, 1978.
4. Frank J. McHugh, Ross Clark, and Mary Soloman, "Wind Tunnel Investigation of Rotor Lift and Propulsive Force at High Speeds—Data Analysis," NASA CR 145217-1, October 1977.
5. F. J. Davenport and J. V. Front, "Airfoil Sections for Rotor Blades—A Reconsideration," American Helicopter Society 22nd Annual Forum, Washington, D.C., May 12, 1966.
6. John L. McCloud III and George B. McCullough, "Wind-Tunnel Tests of a Full-Scale Helicopter Rotor with Symmetrical and with Cambered Blade Sections at Advance Ratios from 0.3 to 0.4," NASA TN 4367, September 1958.
7. W. J. McCroskey, "Some Current Research in Unsteady Fluid Dynamics—The 1976 Freeman Scholar Lecture," *Journal of Fluids Engineering*, Vol. 99, March 1977, pp. 8–38.
8. Lawrence W. Carr, "Progress in Analysis and Prediction of Dynamic Stall," *Journal of Aircraft*, Vol. 25, No. 1, January 1988, pp. 6–17.
9. W. J. McCroskey, K. W. McAlister, L. W. Carr, and S. L. Pucci, "An Experimental Study of Dynamic Stall on Advanced Airfoil Sections Volume 1. Summary of Experiments," NASA TM 84245, July 1982.
10. K. W. McAlister, S. L. Pucci, W. J. McCroskey, and L. W. Carr, "An Experimental Study of Dynamic Stall on Advanced Airfoil Sections Volume 2. Pressure and Force Data," NASA TM 84245, September 1982.
11. L. W. Carr, W. J. McCroskey, K. W. McAlister, S. L. Pucci, and O. Lambert, "An Experimental Study of Dynamic Stall on Advanced Airfoil Sections Volume 3. Hot-Wire and Hot-Film Measurements," NASA TM 84245, December 1982.
12. William G. Bousman, "A Qualitative Examination of Dynamic Stall from Flight Test Data," American Helicopter Society 53rd Annual Forum Proceedings, Virginia Beach, VA, April 29-May 1, 1997, pp. 368–387.
13. D. Jepson, R. Moffitt, K. Hilzinger, and J. Bissell, "Analysis and Correlation of Test Data From an Advanced Technology Rotor System," NASA CR 3714, 1983.
14. Charles E. K. Morris, Jr., Robert L. Tomaine, and Darlene D. Stevens, "A Flight Investigation of Performance and Loads for a Helicopter with NLR–1T Main-Rotor Blade Sections," NASA TM 80165, October 1979.
15. Charles E. K. Morris, Jr., Robert L. Tomaine, and Darlene D. Stevens, "A Flight Investigation of Blade-Section Aerodynamics for a Helicopter with NLR–1T Airfoil Sections," NASA TM 80166, January 1980.
16. A. O. St. Hilaire, F. O. Carta, M. R. Fink, and W. D. Jepson, "The Influence of Sweep on the Aerodynamic Loading of an Oscillating NACA 0012 Airfoil. Volume I – Technical Report," NASA CR-3092, February, 1979.
17. Santu T. Gangwani, "Prediction of Dynamic Stall and Unsteady Airloads for Rotor Blades," American Helicopter Society 37th Annual Forum Proceedings, New Orleans, LA, May 17-20, 1981, pp. 1–17.
18. J. Renaud and J. Coulomb, "2D Simulation of Unsteady Phenomena on a Rotor," Paper No. 10, Fourth European Rotorcraft and Powered Lift Forum, Stresa, Italy, September 13-15, 1978.
19. K. W. McAlister and C. Tung, "Suppression of Dynamic Stall with a Leading-Edge Slat on a VR–7 Airfoil," NASA TP 3357, March 1993.
20. L. U. Dadone, "Two-Dimensional Wind Tunnel Test of an Oscillating Rotor Airfoil, Volume I," NASA CR-2914, December 1977.
21. L. U. Dadone, "Two-Dimensional Wind Tunnel Test of an Oscillating Rotor Airfoil, Volume II," NASA CR-2915, December 1977.
22. Peter F. Lorber and Franklin O. Carta, "Unsteady Stall Penetration Experiments at High Reynolds Number," AFOSR TR-87-1202, April 1987.
23. Robert J. Flemming, "An Experimental Evaluation of Advanced Rotorcraft Airfoils in the NASA Ames Eleven-Foot Wind Tunnel," NASA CR 166587, September 1984.

24. K. W. Washuta and B. P. Stocker, "Air-to-Air Combat Test (AACT II) Maneuvering Flight Loads for UH-60A and AUH-76 Helicopters," USAAVSCOM TR-86-D-1, April 1986.
25. Robert M. Kufeld and Wayne Johnson, "The Effects of Control System Stiffness Models on the Dynamic Stall Behavior of a Helicopter," AHS International 54th Annual Forum Proceedings, Washington, D.C., May 20-22, 1998, pp. 589-601.
26. Keith W. Robinson and J. Gordon Leishman, "Effects of Ballistic Damage on the Aerodynamics of Helicopter Rotor Airfoils," *Journal of Aircraft*, Vol. 35, No. 5, September-October 1998.
27. Thomas H. Maier and William G. Bousman, "An Examination of the Aerodynamic Moment on Rotor Blade Tips Using Flight Test Data and Analysis," Paper No. 48, Eighteenth European Rotorcraft Forum, Avignon, France, September 15-18, 1992.
28. Robert M. Kufeld, Dwight L. Balough, Jeffrey L. Cross, Karen F. Studebaker, Christopher D. Jennison, and William G. Bousman, "Flight Testing the UH-60A Airloads Aircraft," American Helicopter Society 50th Annual Forum Proceedings, Washington, D.C., May 11-13, 1994, pp. 557-578.
29. Wayne Johnson, *Helicopter Theory*, Princeton University Press, Princeton, New Jersey, 1980.
30. C. M. Tan and L. W. Carr, "The AFDD International Dynamic Stall Workshop on Correlation of Dynamic Stall Models with 3-D Dynamic Stall Data," NASA TM 110375, July 1996.
31. R. A. Piziali, "An Experimental Investigation of 2D and 3D Oscillating Wing Aerodynamics for a Range of Angle of Attack Including Stall," NASA TM 4632, September 1994.
32. J. G. Leishman and T. S. Beddoes, "A Semi-Empirical Model for Dynamic Stall," *Journal of the American Helicopter Society*, Vol. 34, No. 3, July 1989, pp. 3-17.
33. T. S. Beddoes, "Two and Three Dimensional Indicial Methods for Rotor Dynamic Airloads," American Helicopter Society National Specialists' Meeting on Rotorcraft Dynamics, Arlington, TX, November 13-14, 1989.
34. T. S. Beddoes, "A Near-Wake Dynamic Model," American Helicopter Society National Specialists' Meeting on Aerodynamics and Aeroacoustics, Arlington, TX, February 25-27, 1987.
35. J. J. Costes, "Unsteady Three-Dimensional Stall on a Rectangular Wing," Twelfth European Rotorcraft Forum, Garmisch-Partenkirchen, Federal Republic of Germany, September 22-25, 1986.
36. D. Petot, "Differential Equation Modeling of Dynamic Stall," *La Recherche Aéronautique*, No. 1989-5.
37. R. E. Gormont, "A Mathematical Model of Unsteady Aerodynamics and Radial Flow for Application to Helicopter Rotors," USAAVLABS TR 72-67, May 1973.
38. Khanh Nguyen and Wayne Johnson, "Evaluation of Dynamic Stall Models with UH-60A Airloads Flight Test Data," American Helicopter Society 54th Annual Forum Proceedings, Washington, D.C., May 20-22, 1998, pp. 576-587.
39. W. Johnson, "The Response and Airloading of Helicopter Rotor Blades Due to Dynamic Stall," ASRL TR 130-1, May 1970.
40. V. K. Truong, "A 2-D Dynamic Stall Model Based on a Hopf Bifurcation," Nineteenth European Rotorcraft Forum, Cernobbio, Italy, September 14-16, 1993.
41. J. C. Narramore, W. J. McCroskey, and K. W. Noonan, "Design and Evaluation of Multi-Element Airfoils for Rotorcraft," American Helicopter Society 55th Annual Forum Proceedings, Montreal, Canada, May 25-27, 1999, pp. 1960-1970.
42. C. M. Wang, J. C. Wu, and C. Tung, "A Numerical Study of General Viscous Flows Around Multi-Element Airfoils," AIAA Paper 90-0572, January 1990.
43. Yung H. Yu, Soogab Lee, Kenneth W. McAlister, Chee Tung, and Clin M. Wang, "High Lift Concepts for Rotorcraft Applications," American Helicopter Society 49th Annual Forum Proceedings, St. Louis, MO, May 19-21, 1993, pp. 1141-1166.
44. P. Plantin De Hugues, K. W. McAlister, and C. Tung, "Effect of an Extendable Slat on the Stall Behavior of a VR-12 Airfoil," NASA TP 3407, September 1993.
45. G. R. Srinivasan and J. A. Ekaterinaris, "Dynamic Stall of an Oscillating Wing, Part 1: Evaluation of Turbulence Models," AIAA 11th Applied

Aerodynamics Conference, Monterey, CA,  
August 9-11, 1993.

46. R. Hixon, F.-L. Tsung, and L. N. Sankar, "A Comparison of Two Methods for Solving 3-D Unsteady Compressible Viscous Flows," AIAA Paper 93-0537, 31st Aerospace Sciences Meeting and Exhibit, Reno, NV, January 11-14, 1993.
47. O. Rouzaud and A. Plop, "2D Unsteady Navier-Stokes Computations at ONERA for Prediction of Dynamic Stall," Paper AE02, 24th European Rotorcraft Forum, Marseilles, France, September 15-17, 1998.
48. S. Lee, K. W. McAlister, and C. Tung, "Characteristics of Deformable Leading Edge for High Performance Helicopter Rotor," AIAA 93-3526, AIAA 11th Applied Aerodynamics Conference, August 9-11, 1993, Monterey, CA.

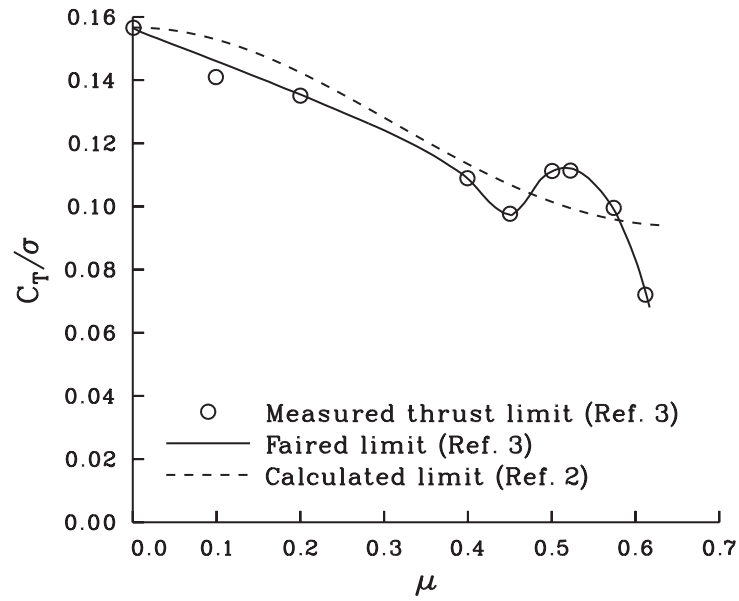


Figure 1. Comparison of measured and calculated limit rotor thrust coefficient as a function of advance ratio for a 10-foot diameter model rotor,  $X/qd^2s = 0.05$ .

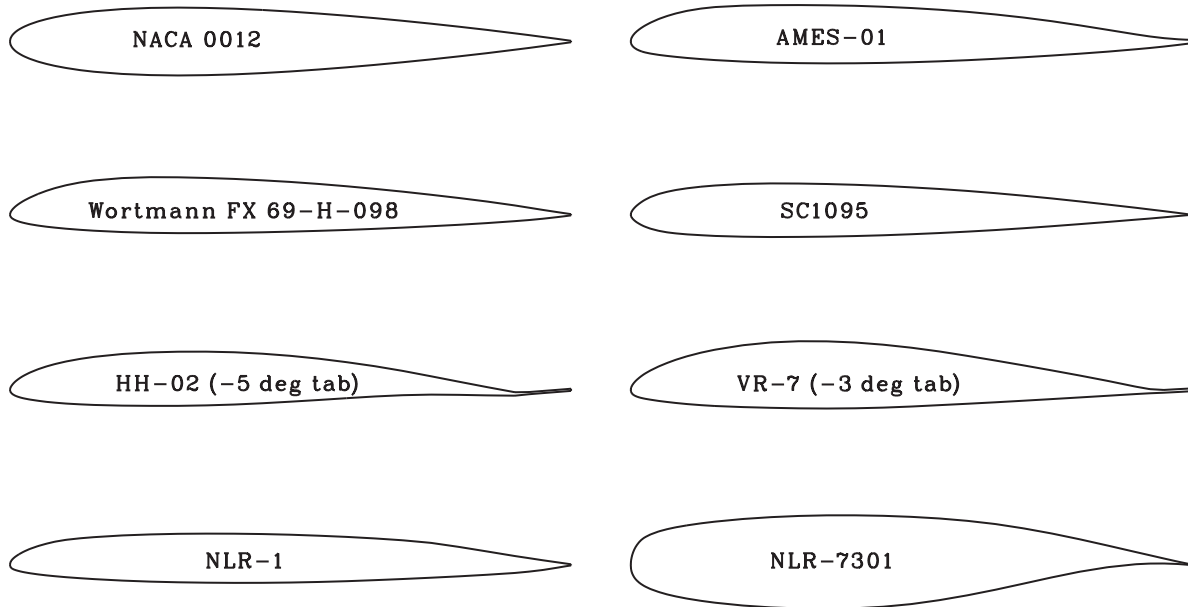


Figure 2. Eight airfoil profiles tested in the NASA Ames 7- by 10-foot wind tunnel (Refs. 9–11).

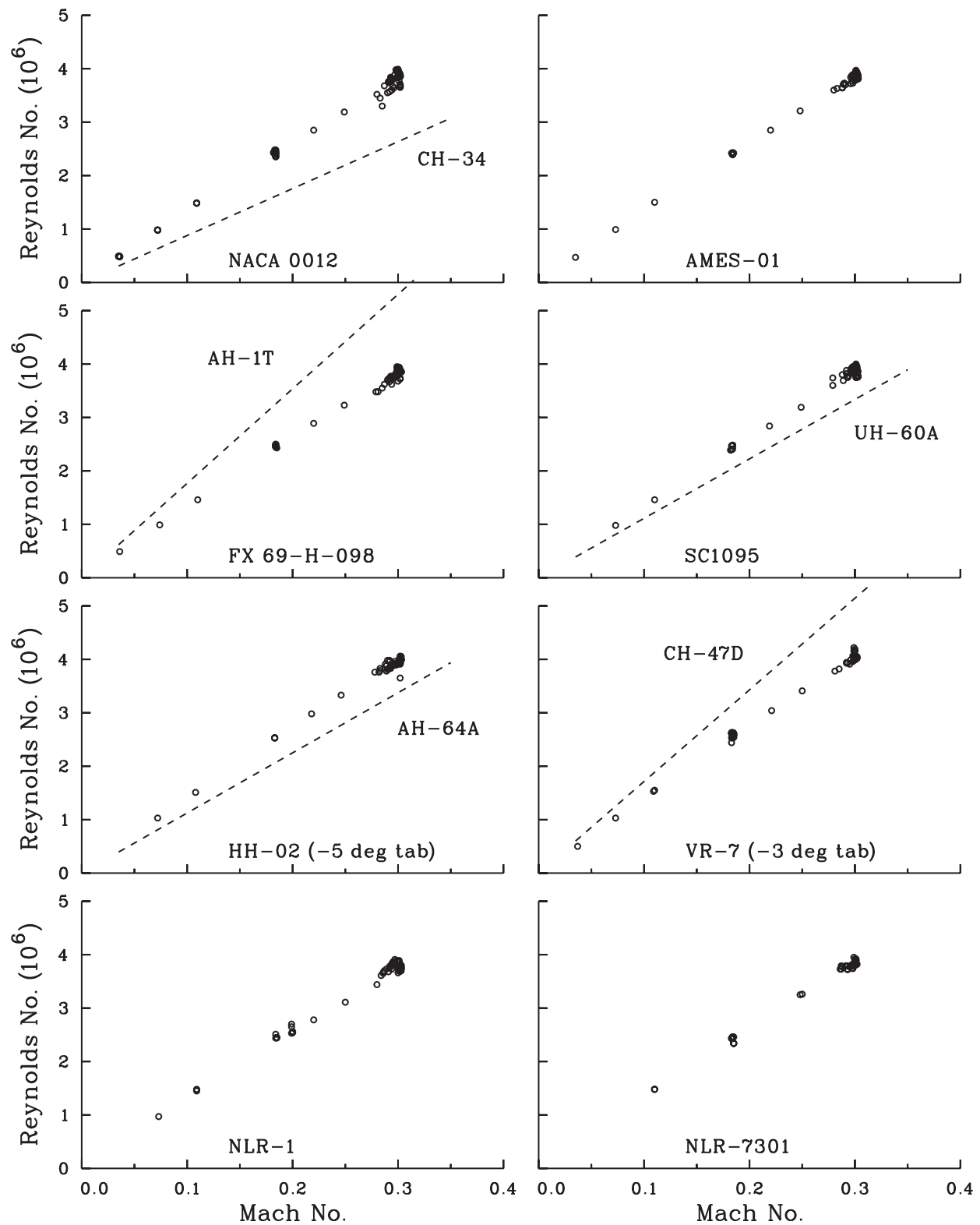


Figure 3. Reynolds and Mach number envelope for Ames dynamic stall tests. Reynolds and Mach number relation for selected aircraft shown with dashed lines.

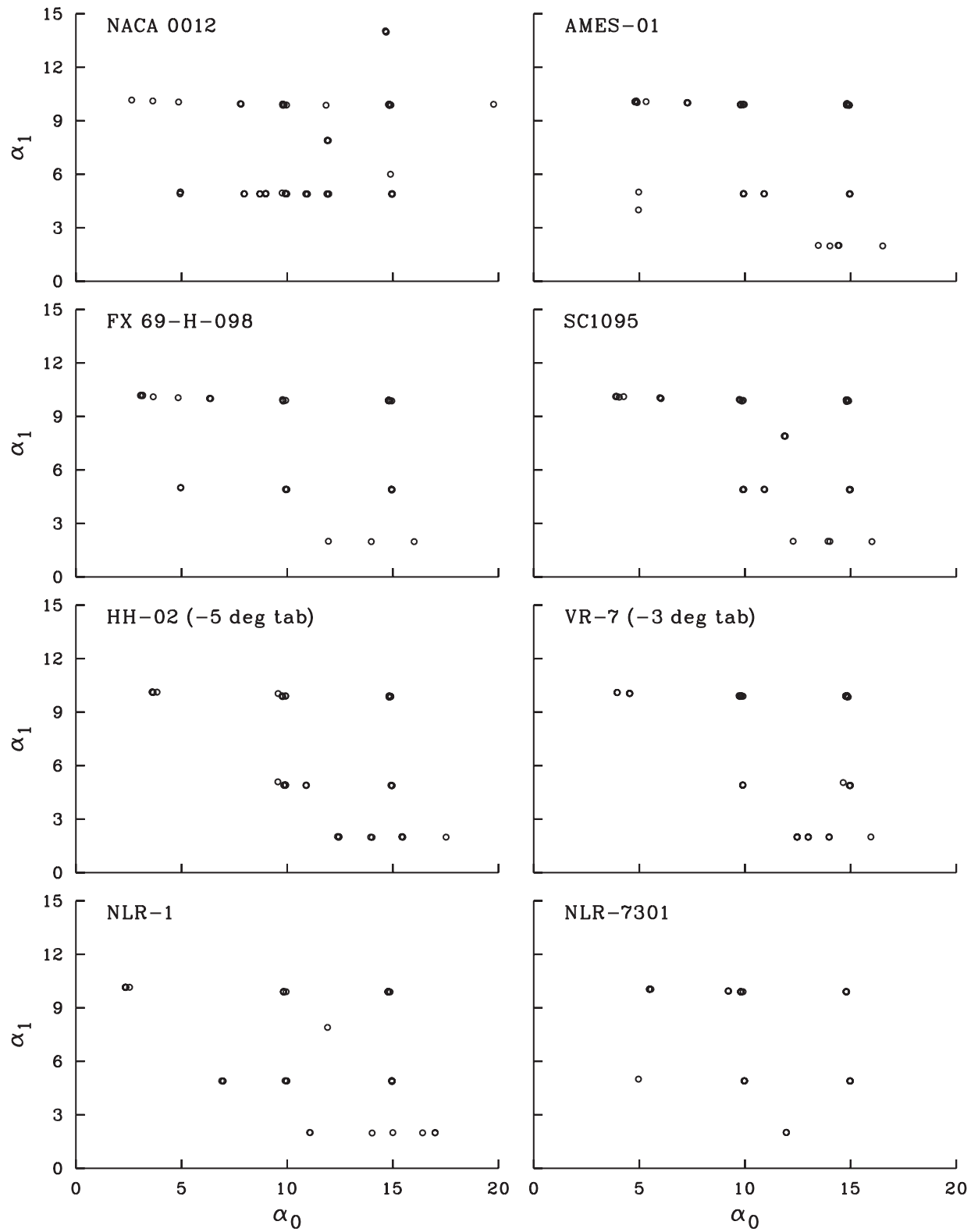


Figure 4. Alternating and steady angles of attack for Ames dynamic stall tests

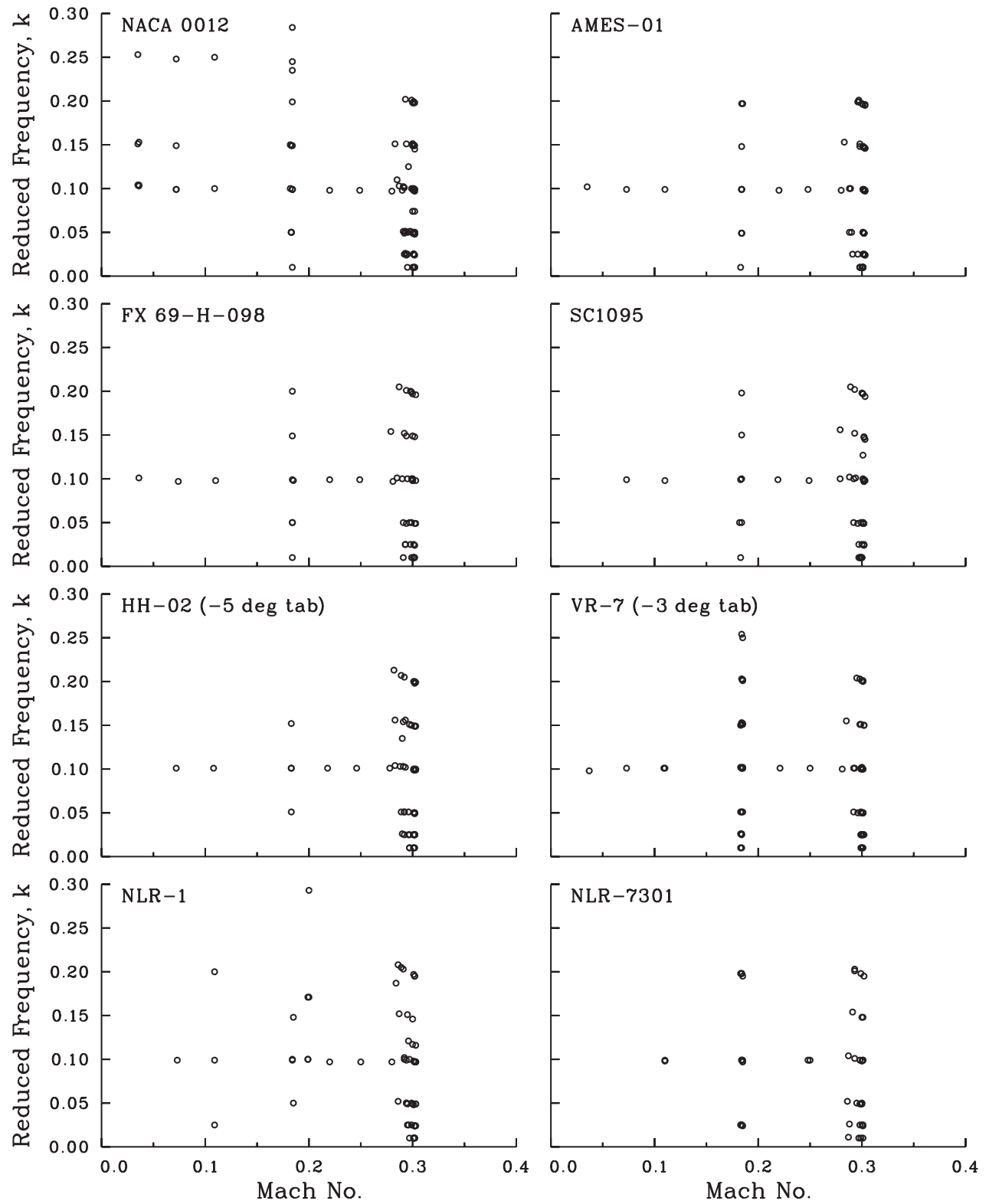


Figure 5. Reduced frequency as a function of Mach number for the Ames dynamic stall tests.



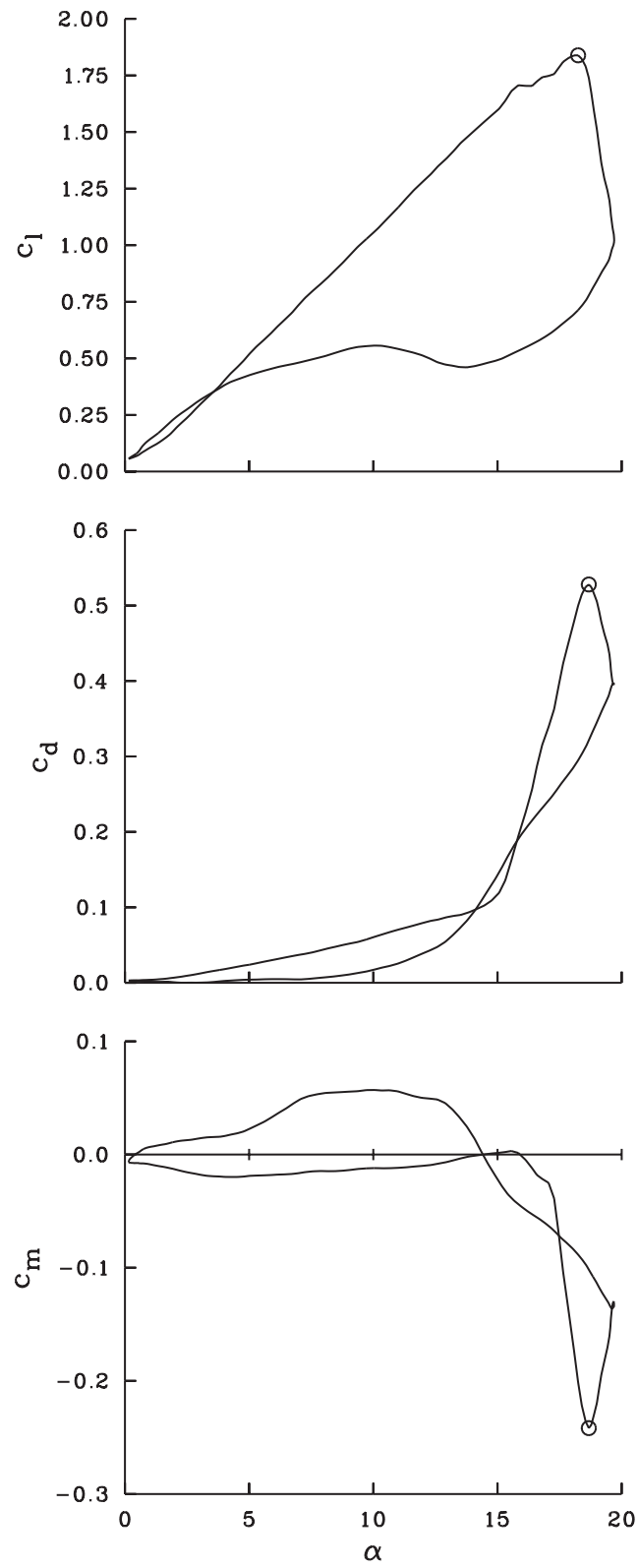


Figure 6. Dynamic stall test point for NACA 0012 from Ames tests; Frame 9302.

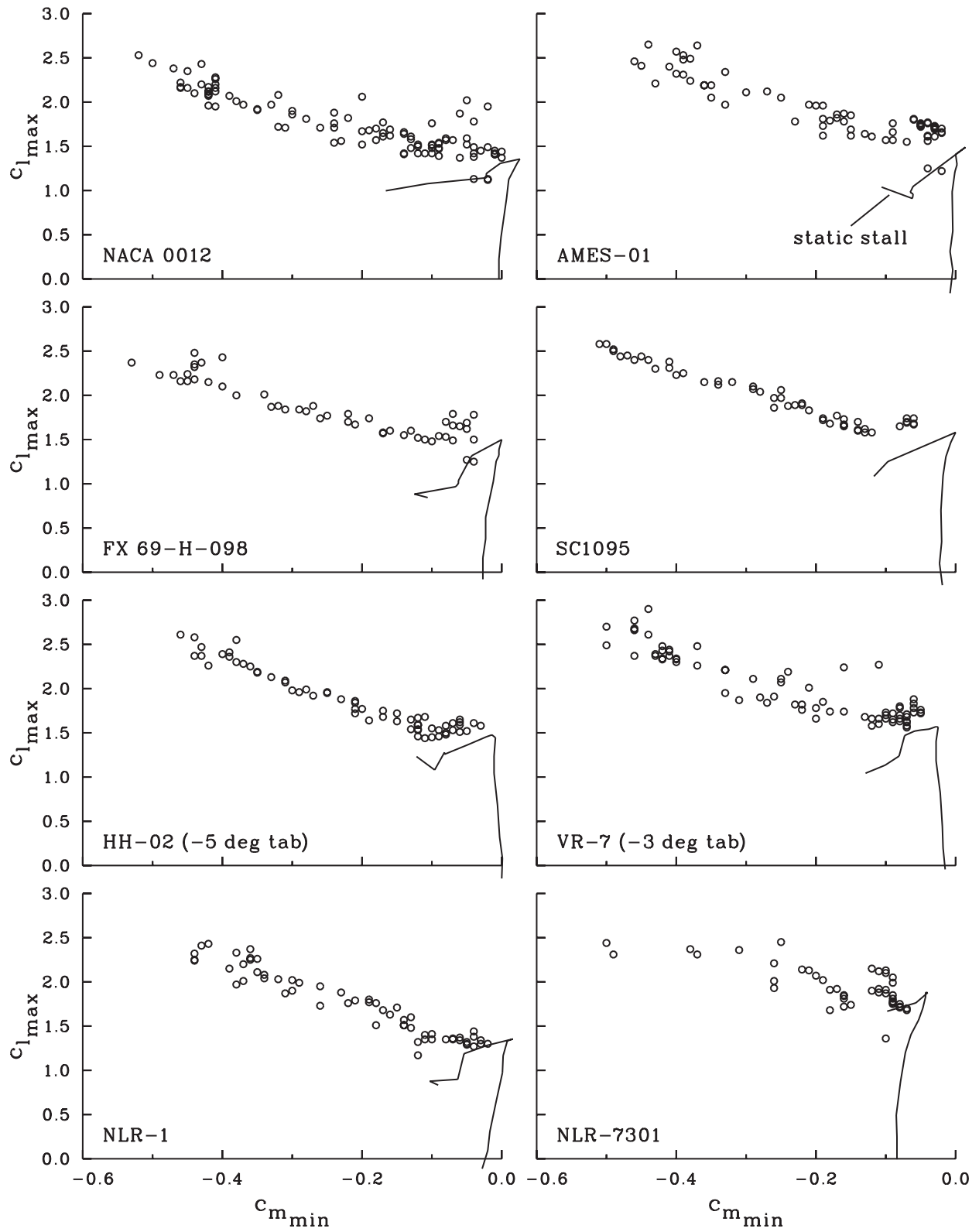


Figure 7. Maximum lift coefficient as a function of minimum moment coefficient for Ames dynamic stall tests (Ref. 9–11).

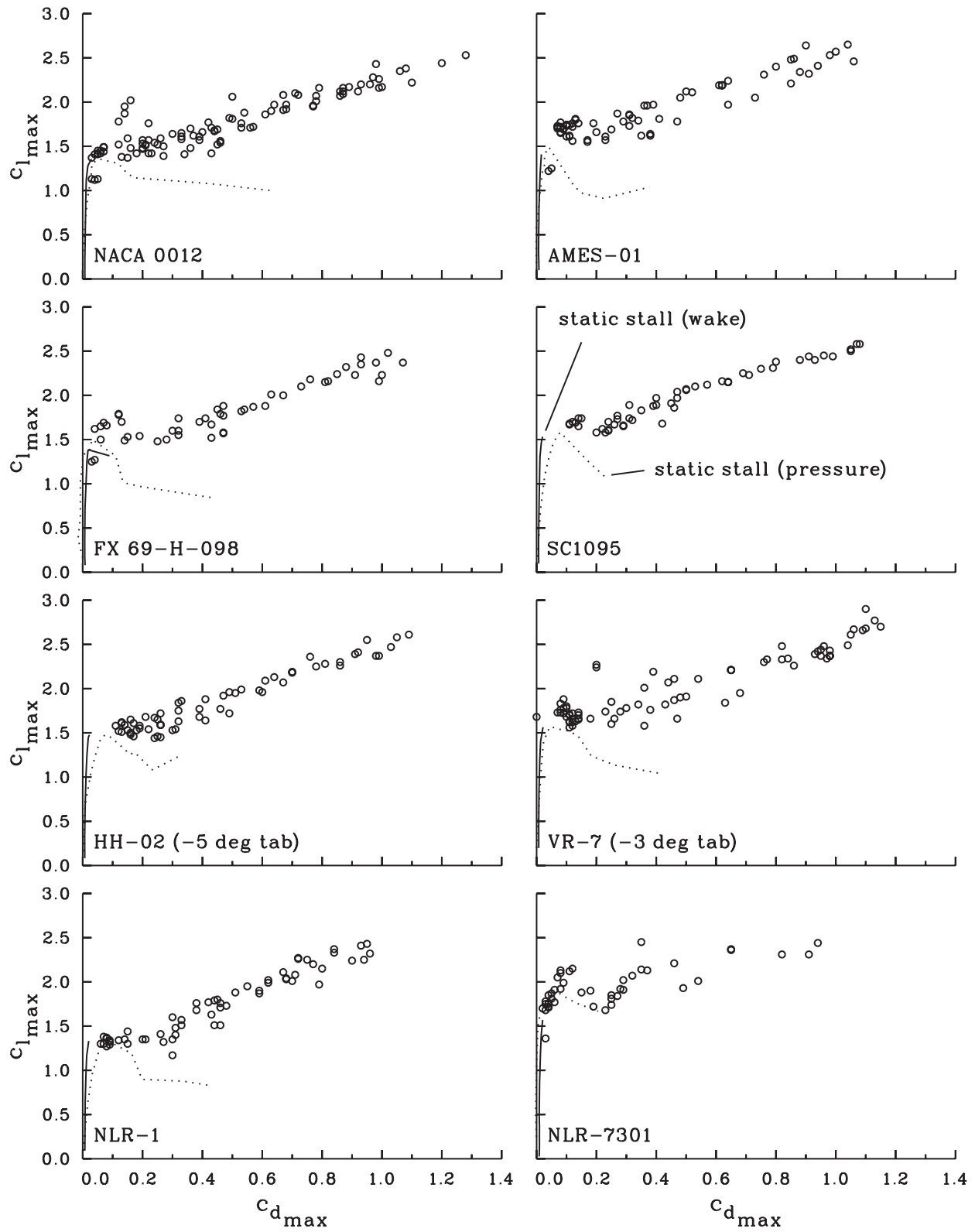


Figure 8. Maximum lift coefficient as a function of maximum drag coefficient for Ames dynamic stall tests (Ref. 9–11).

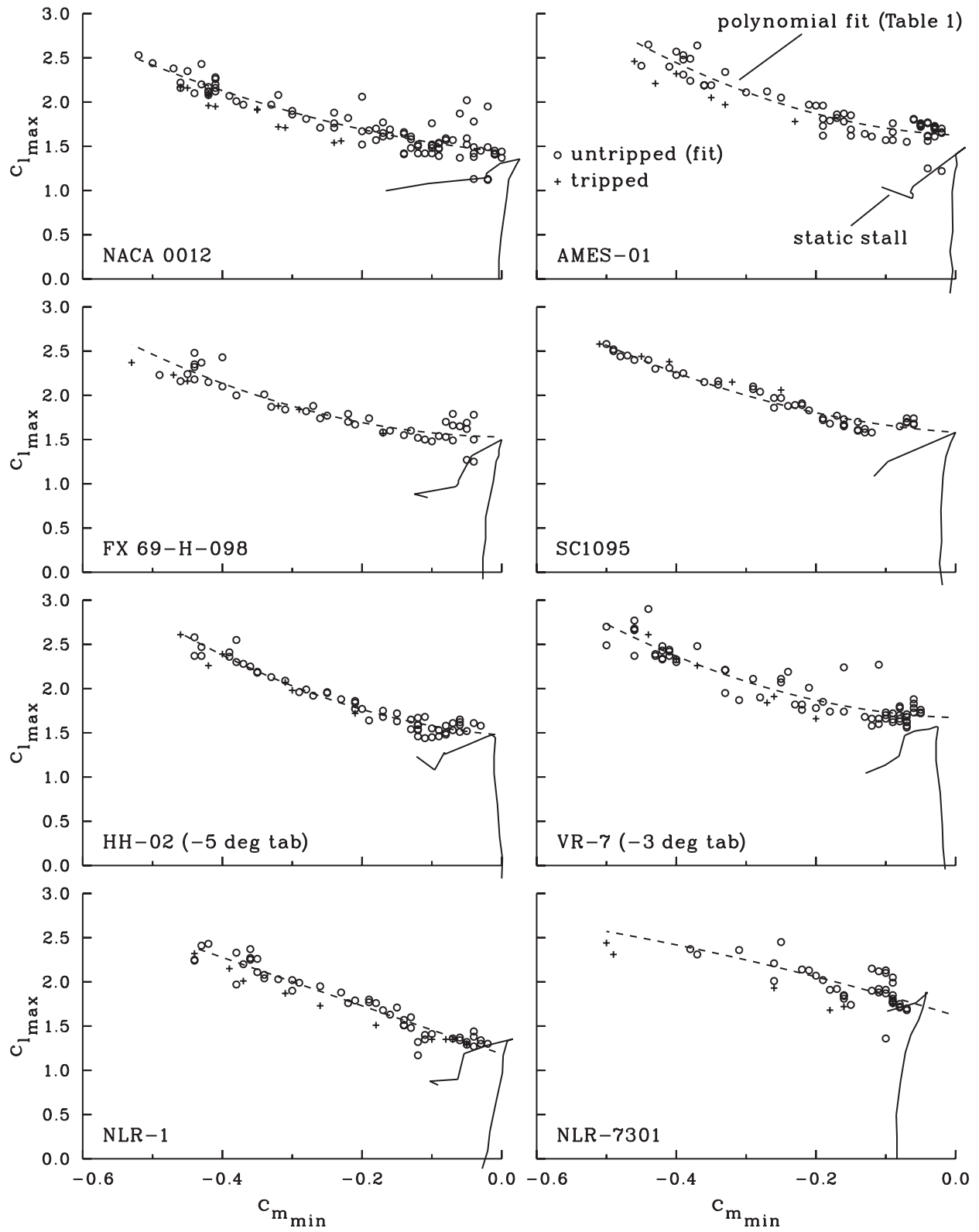


Figure 9. Polynomial fit of maximum lift coefficient as a function of minimum moment coefficient for untripped data from Ames dynamic stall tests (Refs. 9-11).

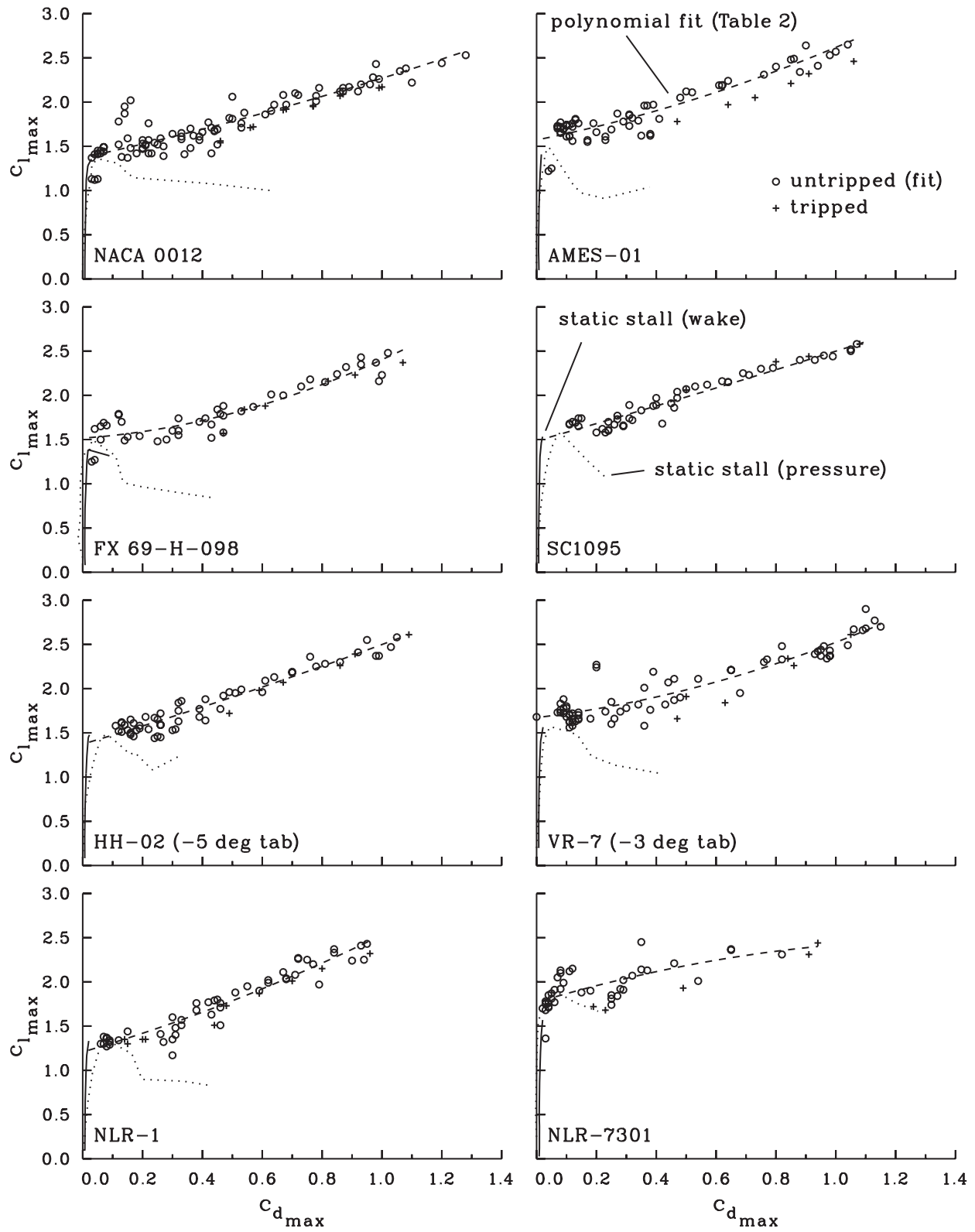


Figure 10. Polynomial fit of maximum lift coefficient as a function of maximum drag coefficient for untripped data from Ames dynamic stall tests (Refs. 9-11).

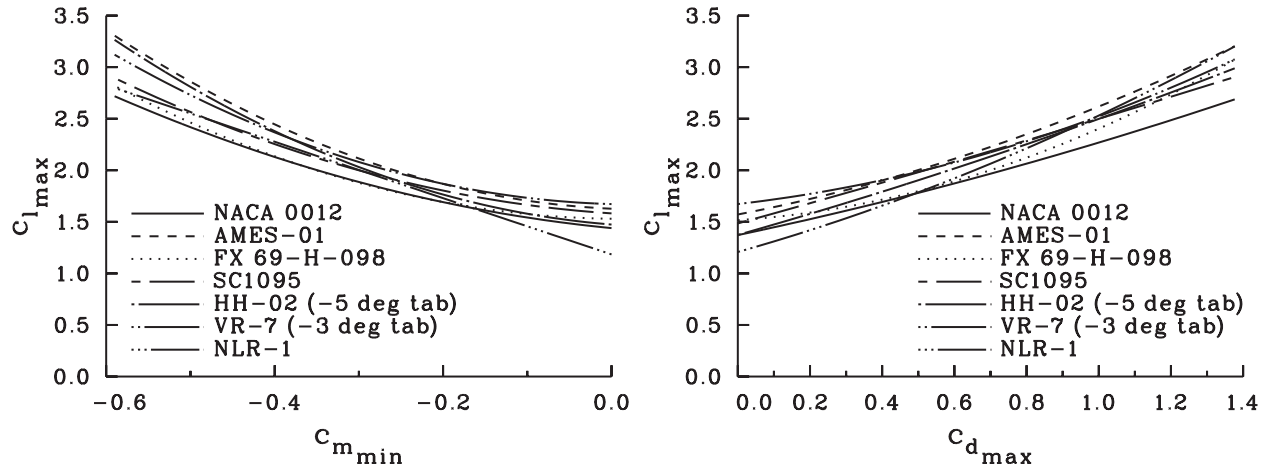


Figure 11. Comparison of dynamic stall functions of seven helicopter airfoil sections.

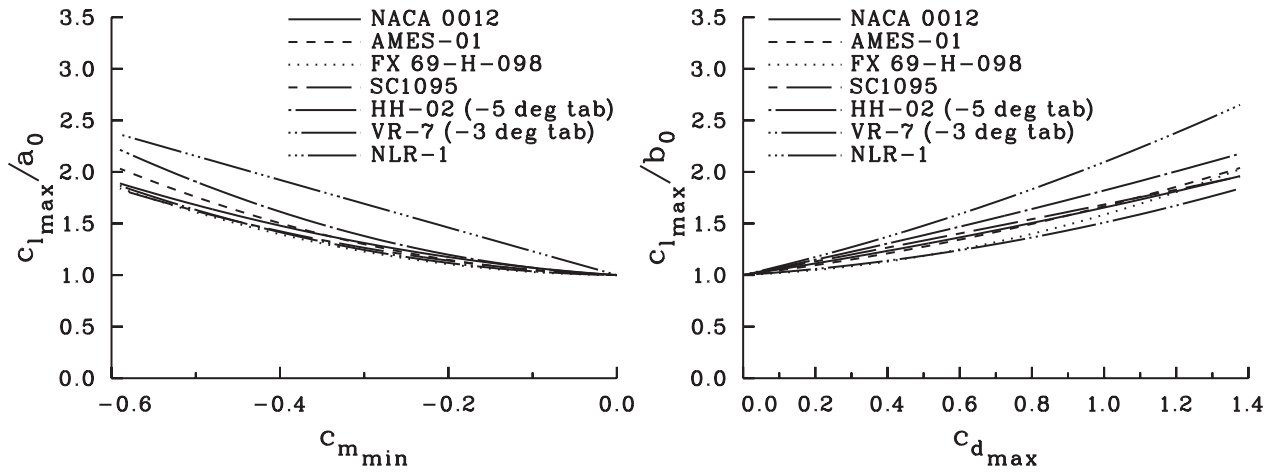


Figure 12. Comparison of normalized dynamic stall functions of seven helicopter airfoil sections.

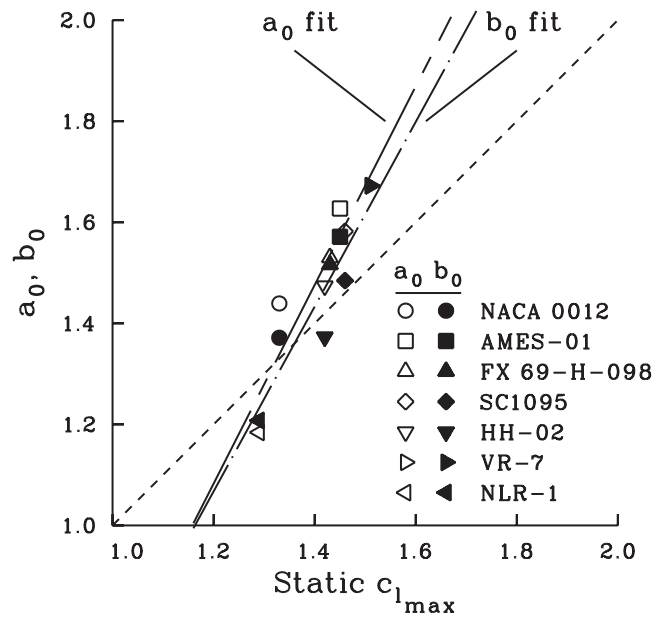


Figure 13. Comparison of polynomial intercepts of dynamic stall functions of seven helicopter airfoils.

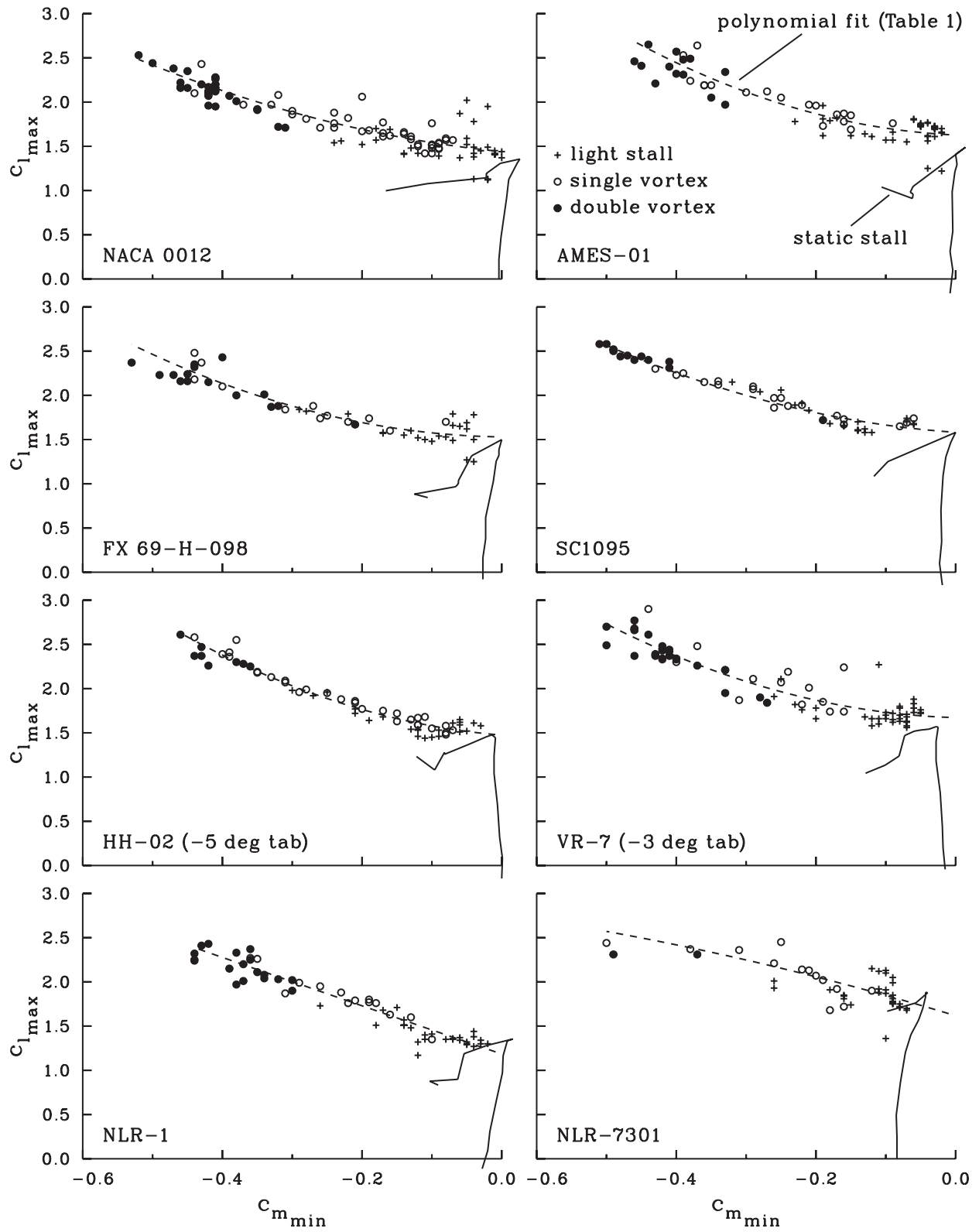


Figure 14. Maximum lift coefficient as a function of minimum moment coefficient showing light dynamic stall, dynamic stall with a single shed vortex, and dynamic stall with two shed vortices.



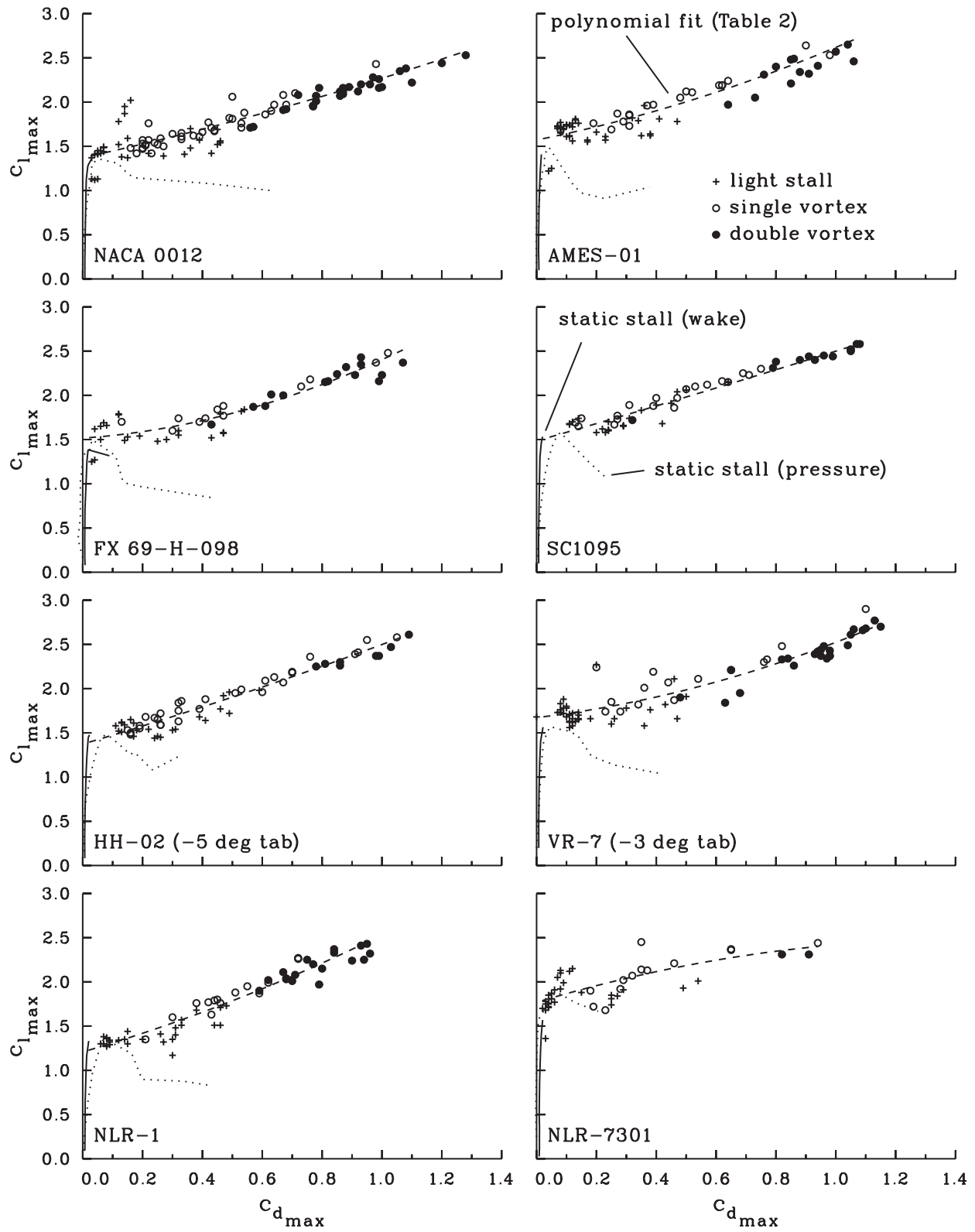


Figure 15. Maximum lift coefficient as a function of maximum drag coefficient showing light dynamic stall, dynamic stall with a single shed vortex, and dynamic stall with two shed vortices.

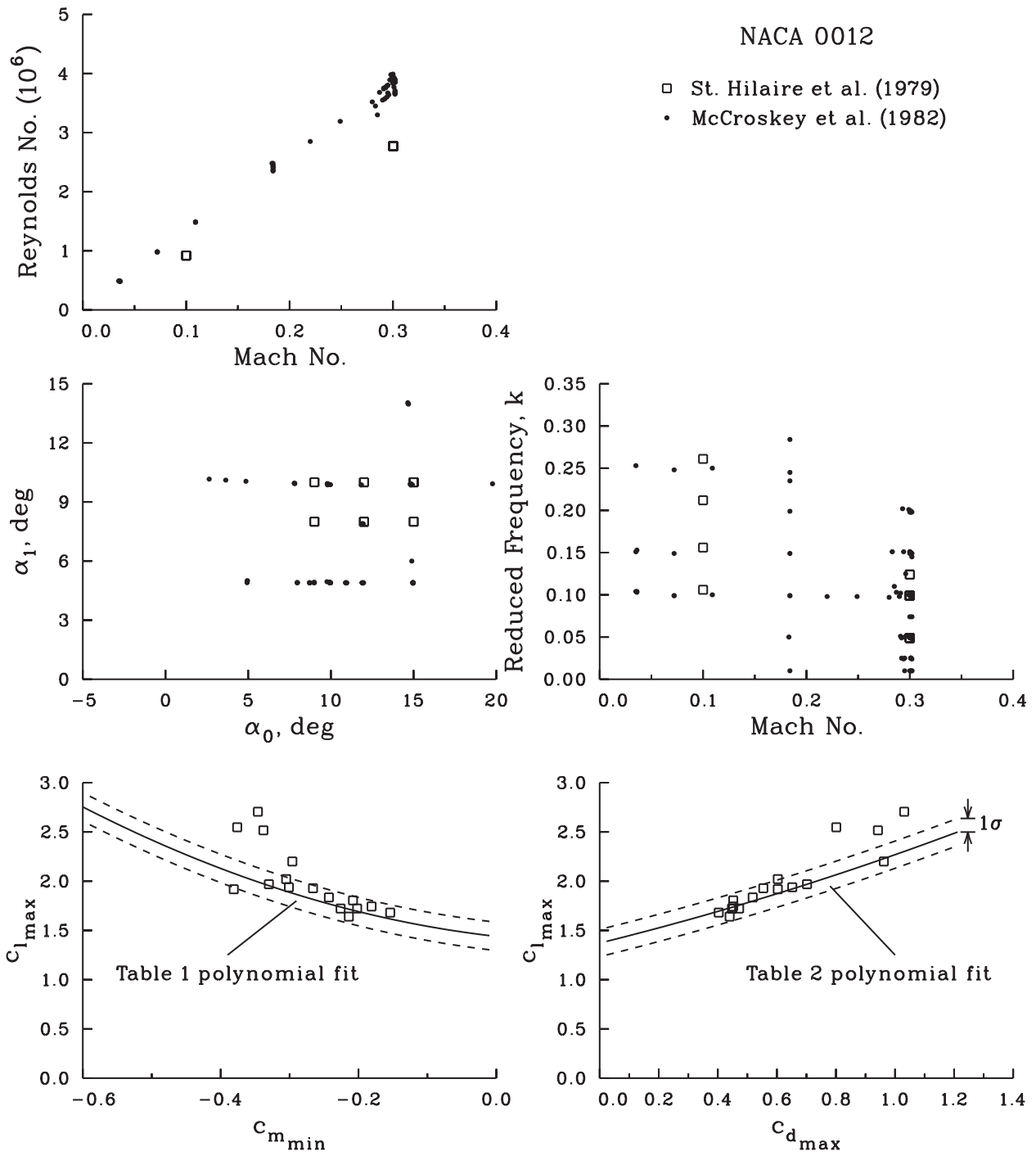


Figure 16. Comparison of UTRC and Ames dynamic stall data for NACA 0012 airfoil.

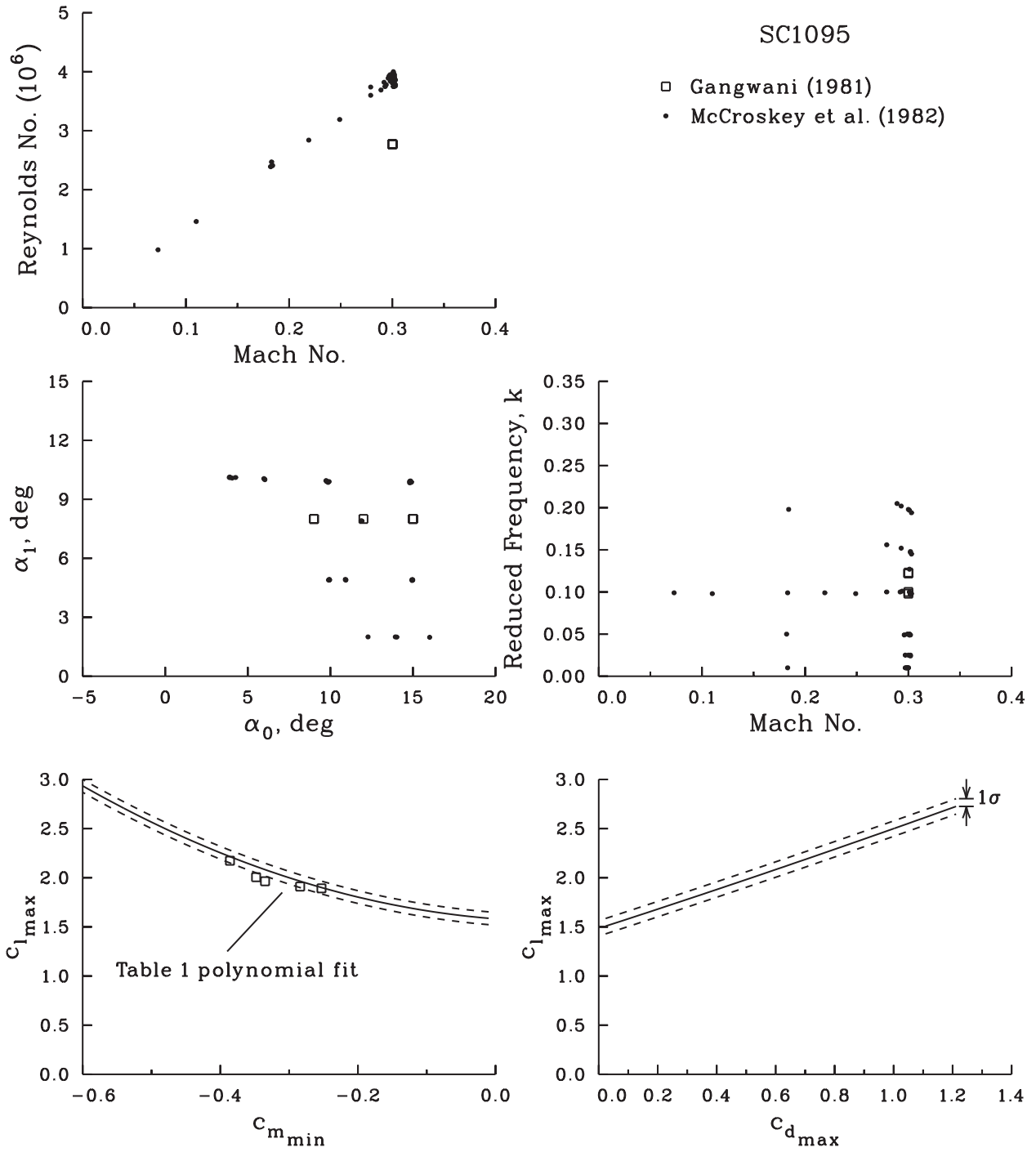


Figure 17. Comparison of UTRC and Ames dynamic stall data for SC1095 airfoil.

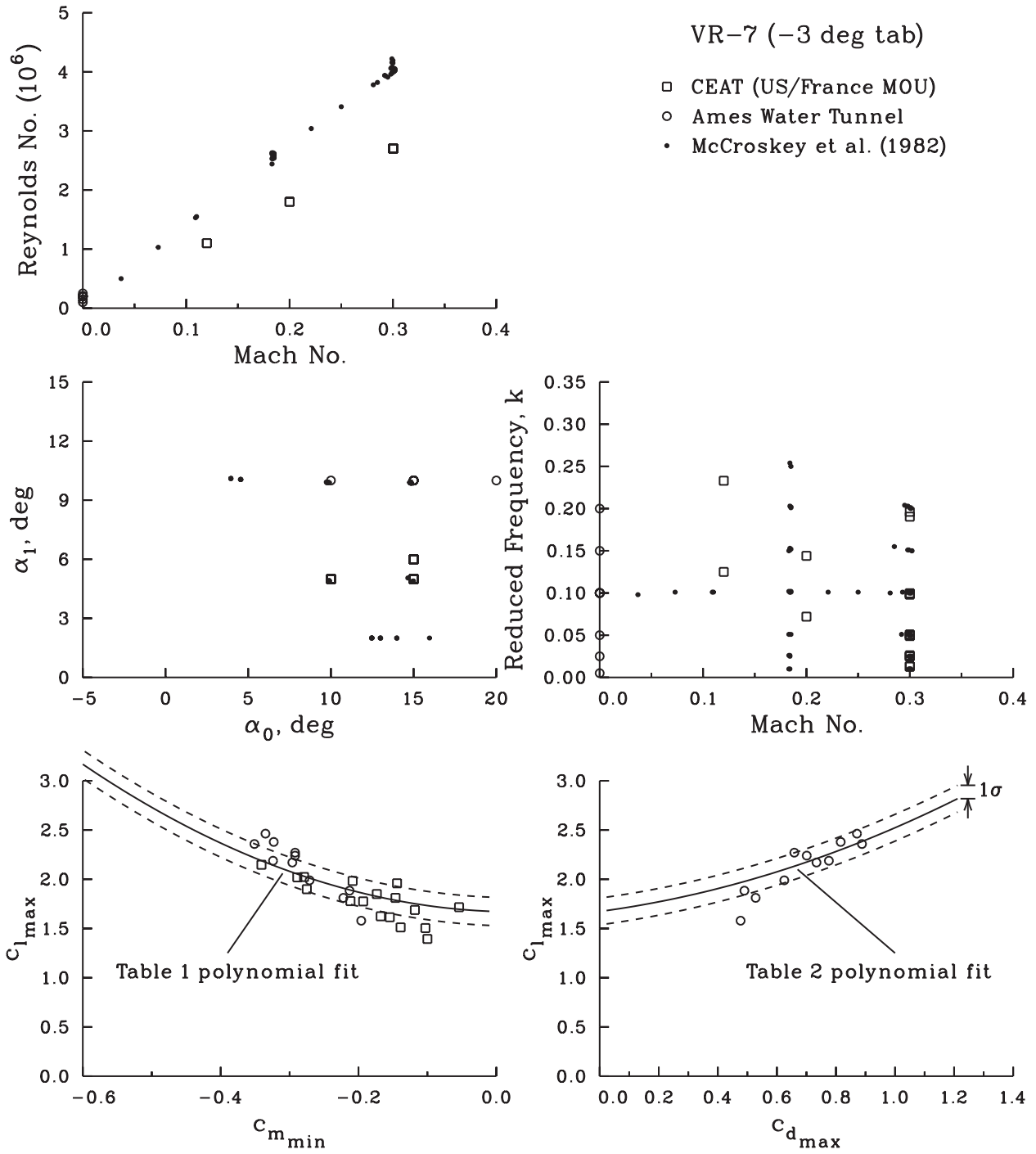


Figure 18. Comparison of CEAT wind tunnel and Ames water tunnel data with Ames wind tunnel dynamic stall data for VR-7 airfoil. CEAT measurements are of maximum normal force coefficient instead of lift coefficient.

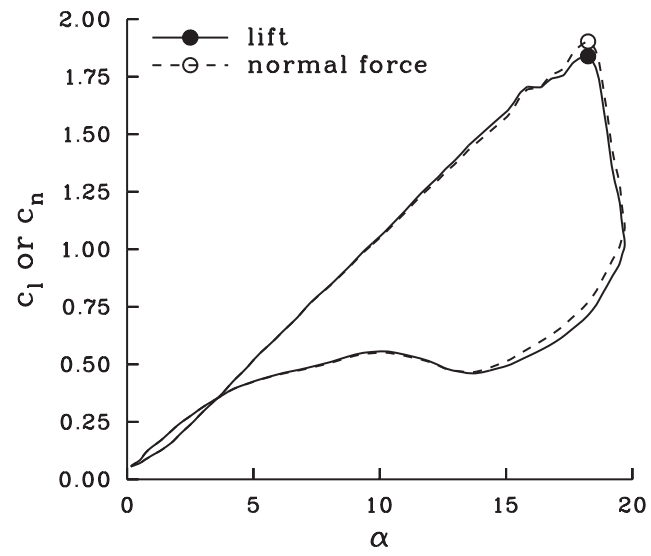


Figure 19. Comparison of lift and normal force coefficients for dynamic stall loop for NACA 0012, Frame 9302..

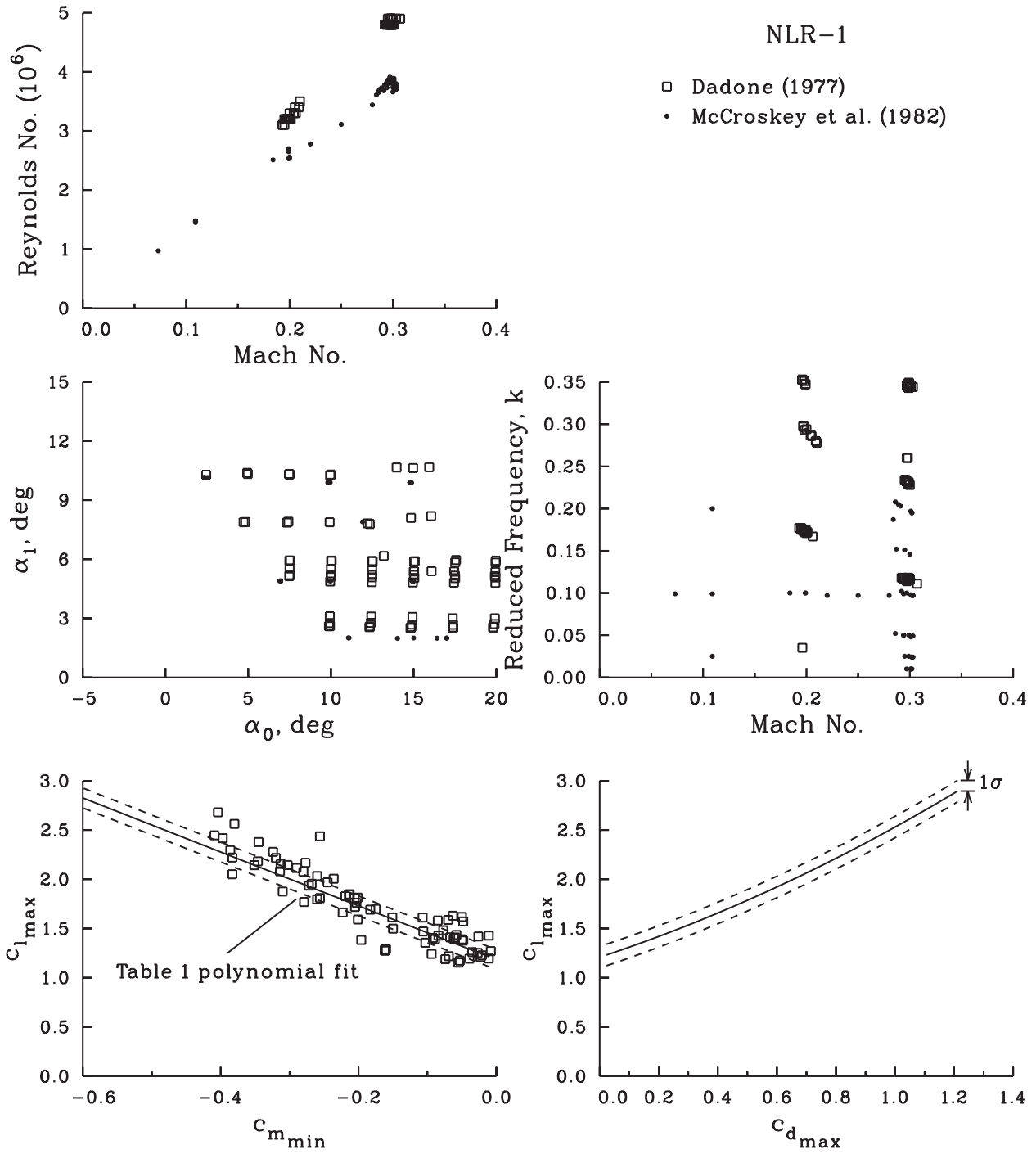


Figure 20. Comparison of BSWT and Ames dynamic stall data for NLR-1 airfoil. BSWT measurements are of maximum normal force coefficient instead of lift coefficient.

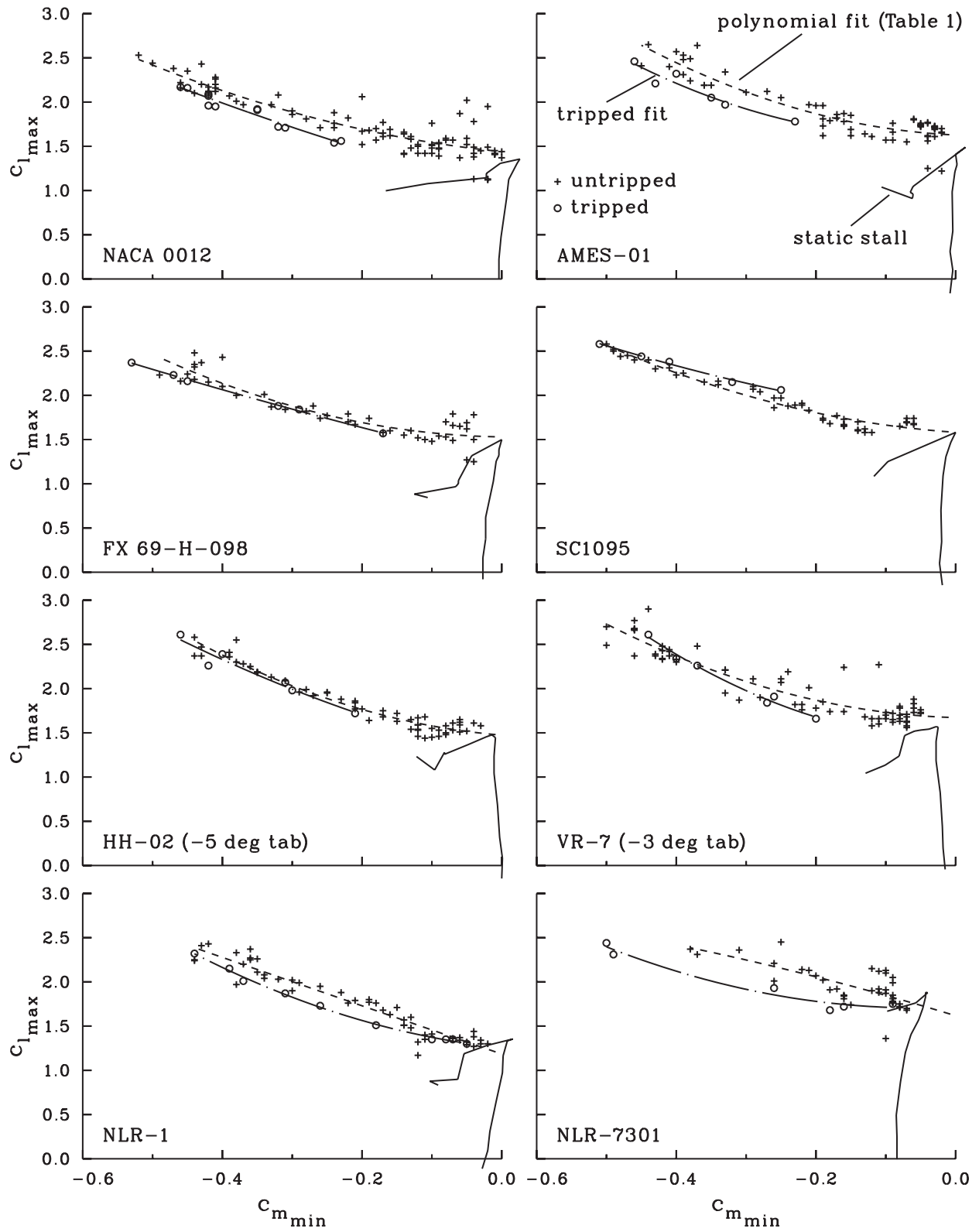


Figure 21. Maximum lift coefficient as a function of minimum moment coefficient showing effect of tripped boundary layer.

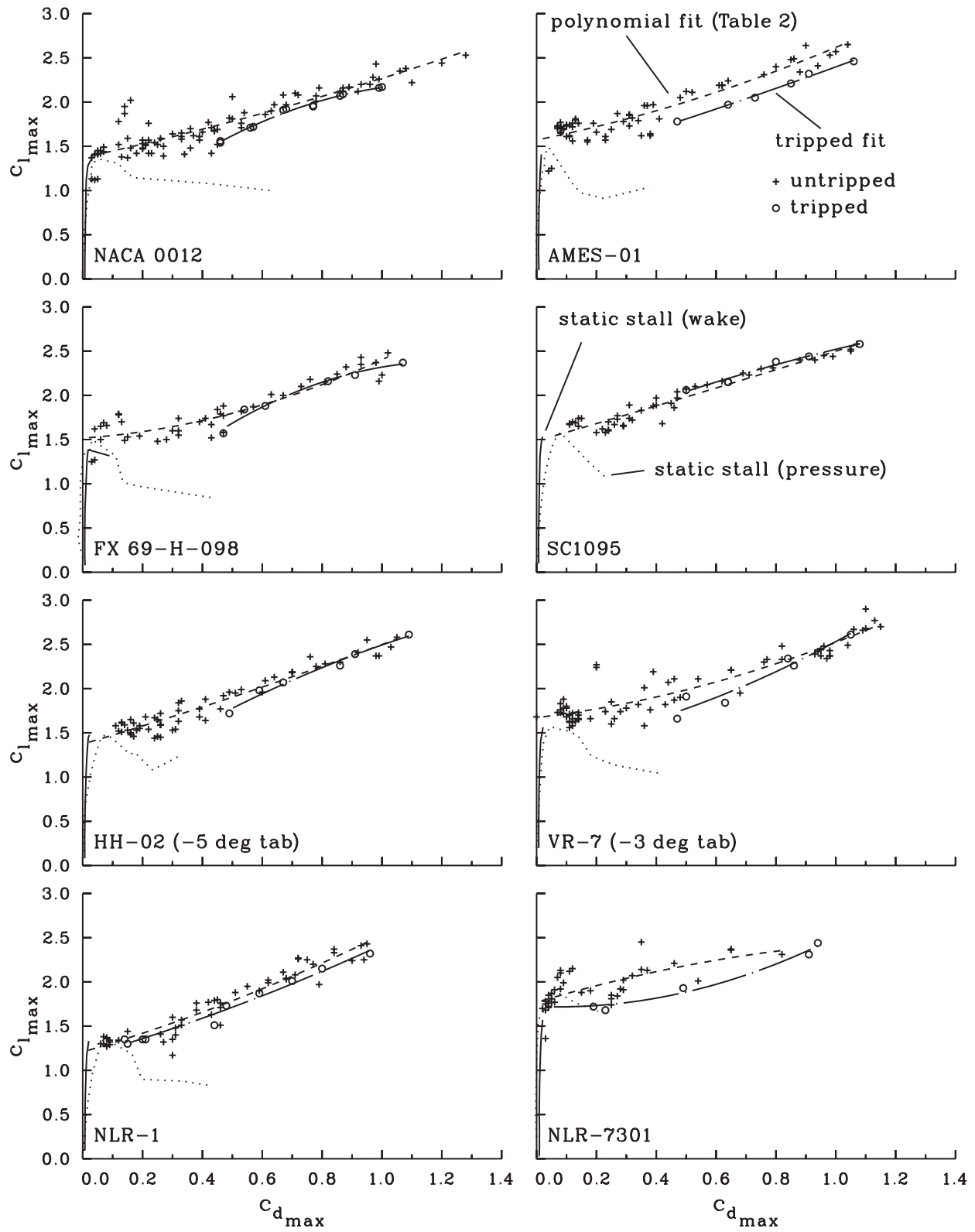


Figure 22. Maximum lift coefficient as a function of maximum drag coefficient showing effect of tripped boundary layer.



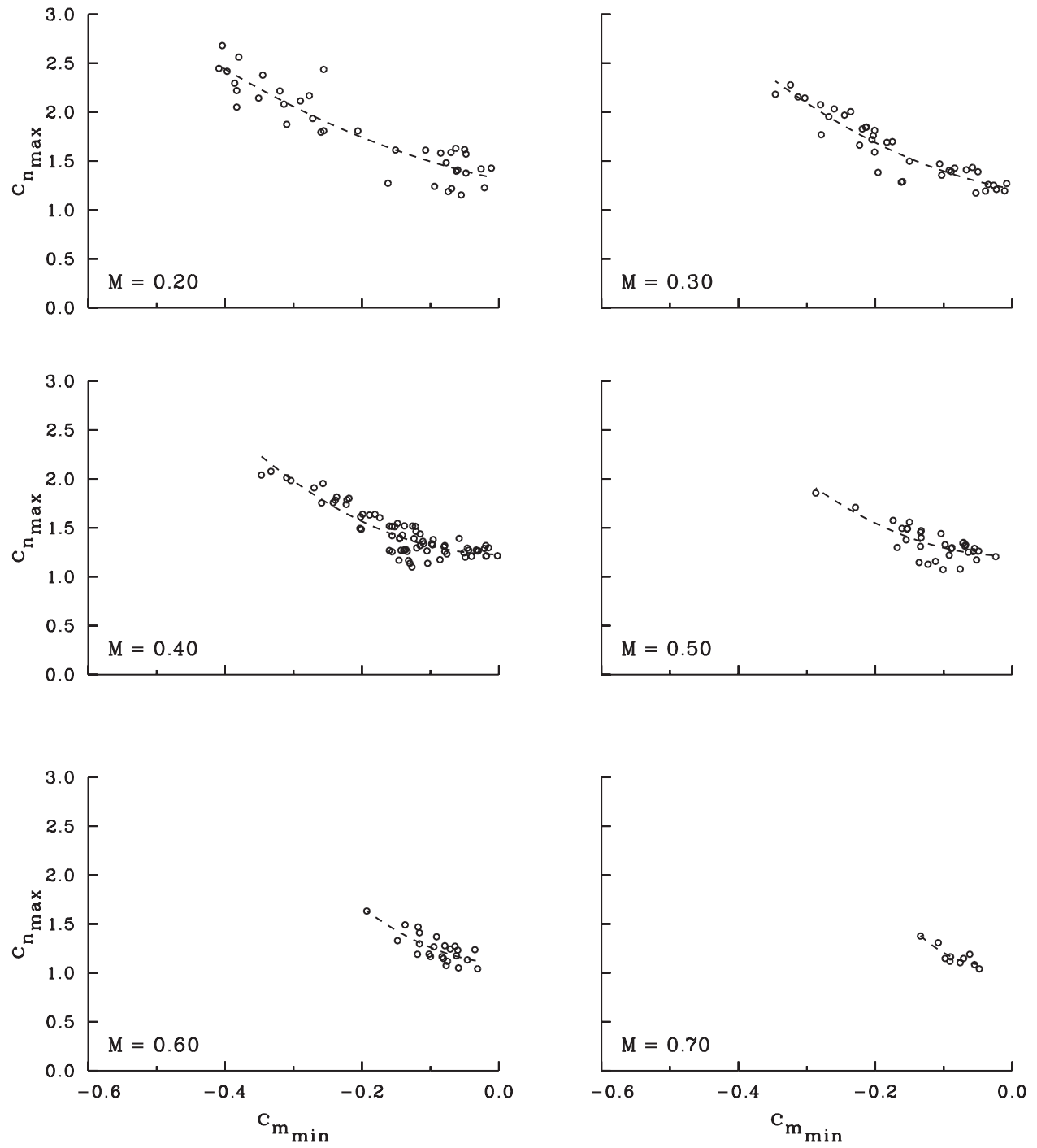


Figure 23. Maximum normal force coefficient as a function of minimum moment coefficient for NLR-1 airfoil at six Mach numbers (Refs. 20, 21).

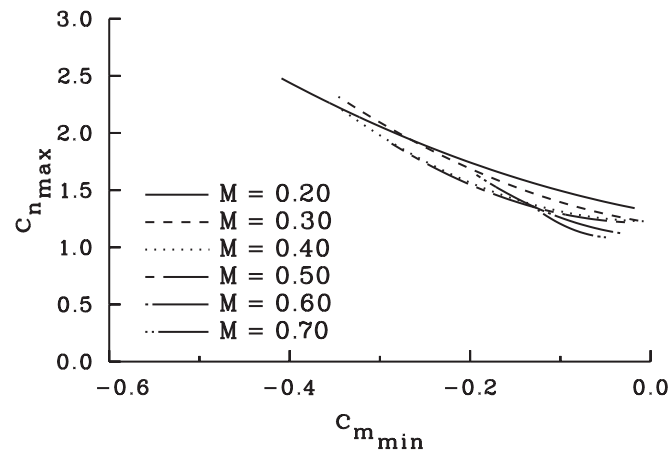


Figure 24. Comparison of polynomial fits for six Mach numbers for NLR-1 airfoil.

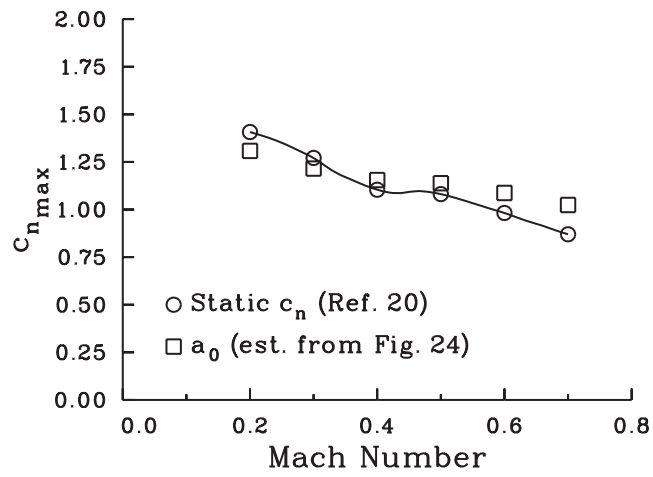


Figure 25. Comparison of best estimate of polynomial fit intercept with static normal force coefficient from wind tunnel measurements (Ref. 20).

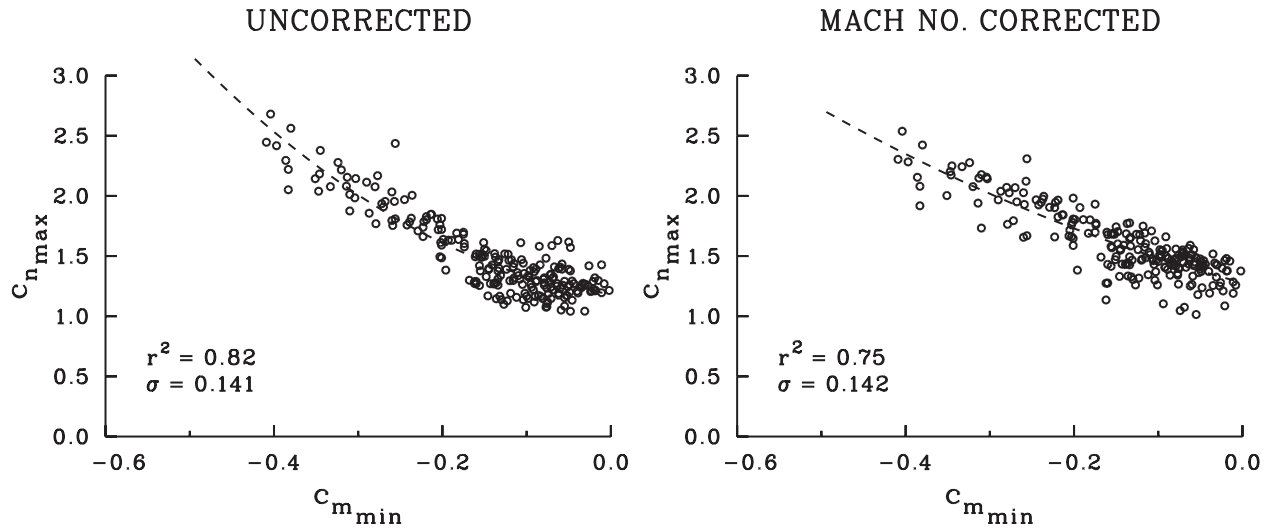


Figure 26. Comparison of uncorrected and corrected maximum normal force coefficient as a function of minimum moment coefficient for NLR-1 airfoil.

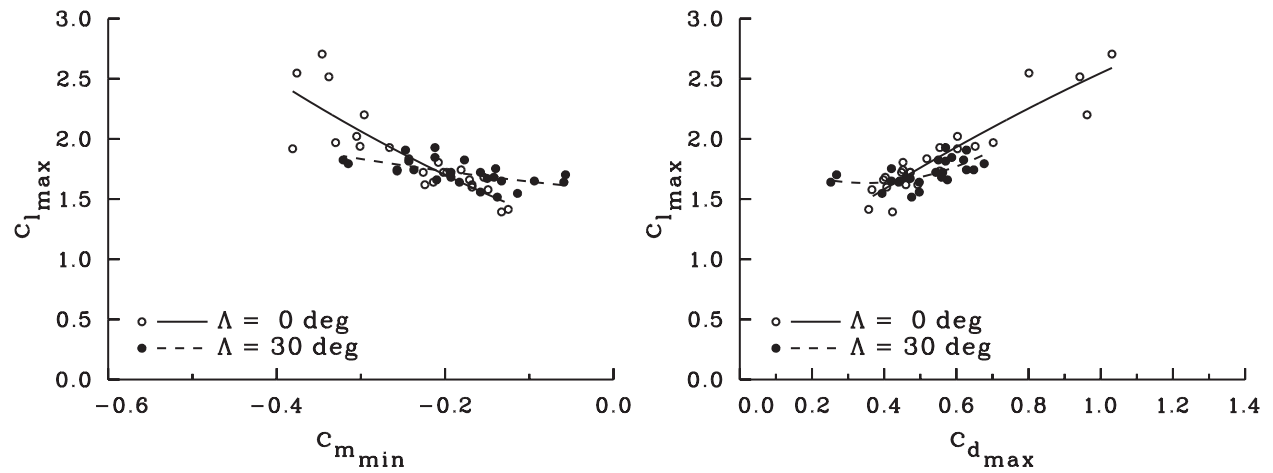


Figure 27. Effect of blade sweep on dynamic stall function for NACA 0012 airfoil (Ref. 16).

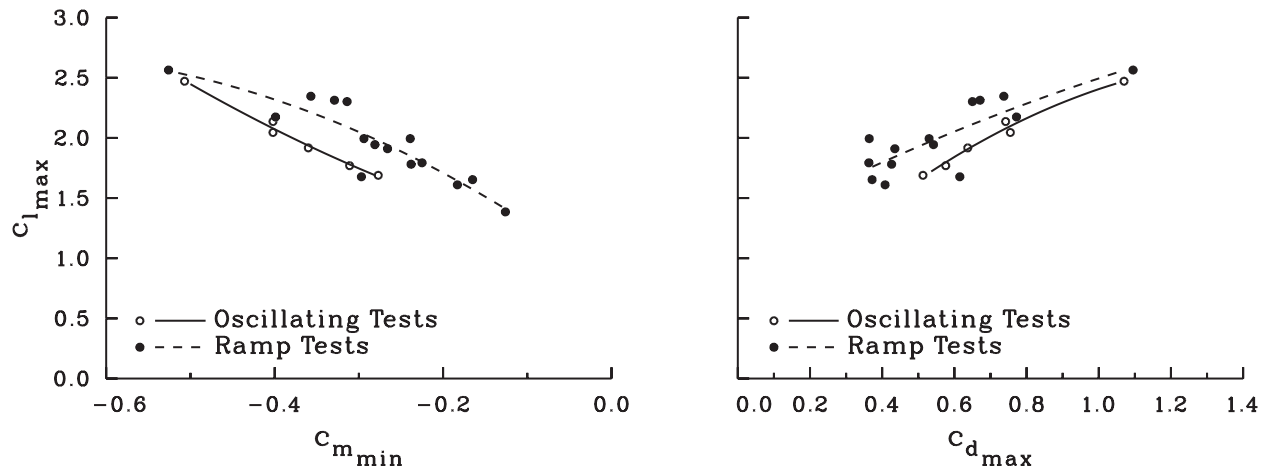


Figure 28. Comparison of dynamic stall functions for SSC-A09 airfoil using oscillating and ramp forcing methods (Ref. 22).

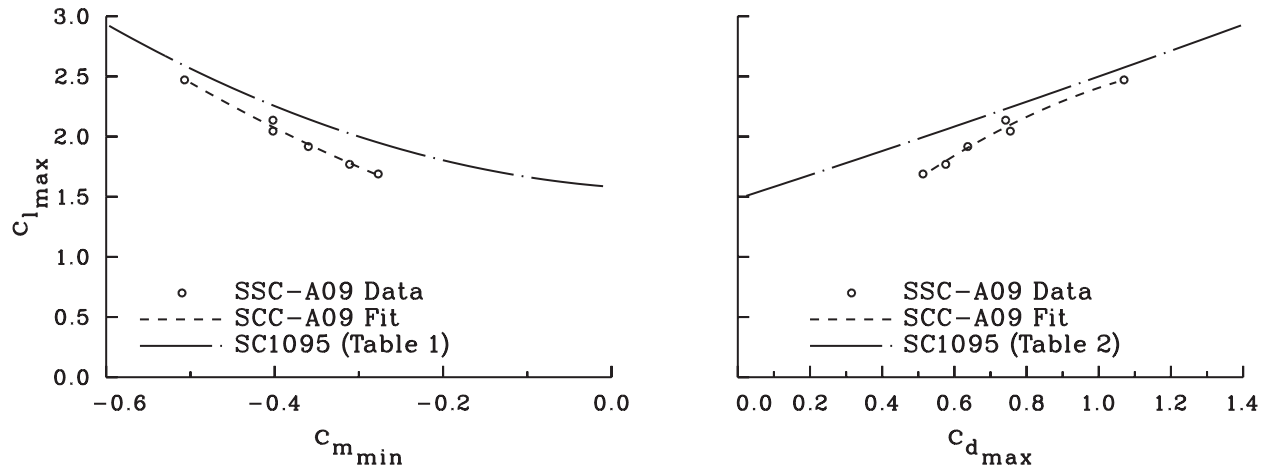


Figure 29. Comparison of SSC-A09 and SC1095 airfoil dynamic stall functions.

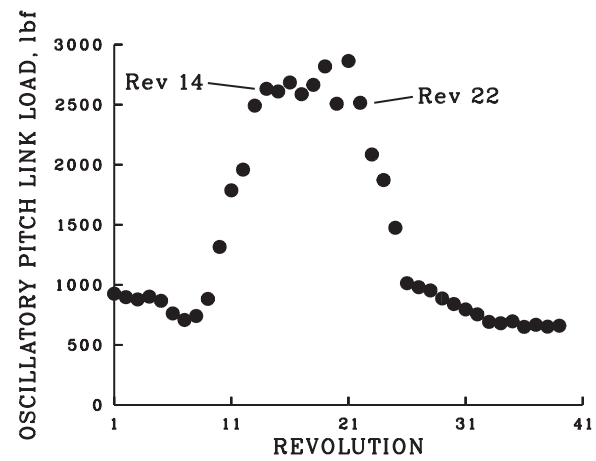


Figure 30. UH-60A oscillatory pitch-link loads in the UTTAS pull-up (Ref. 12).

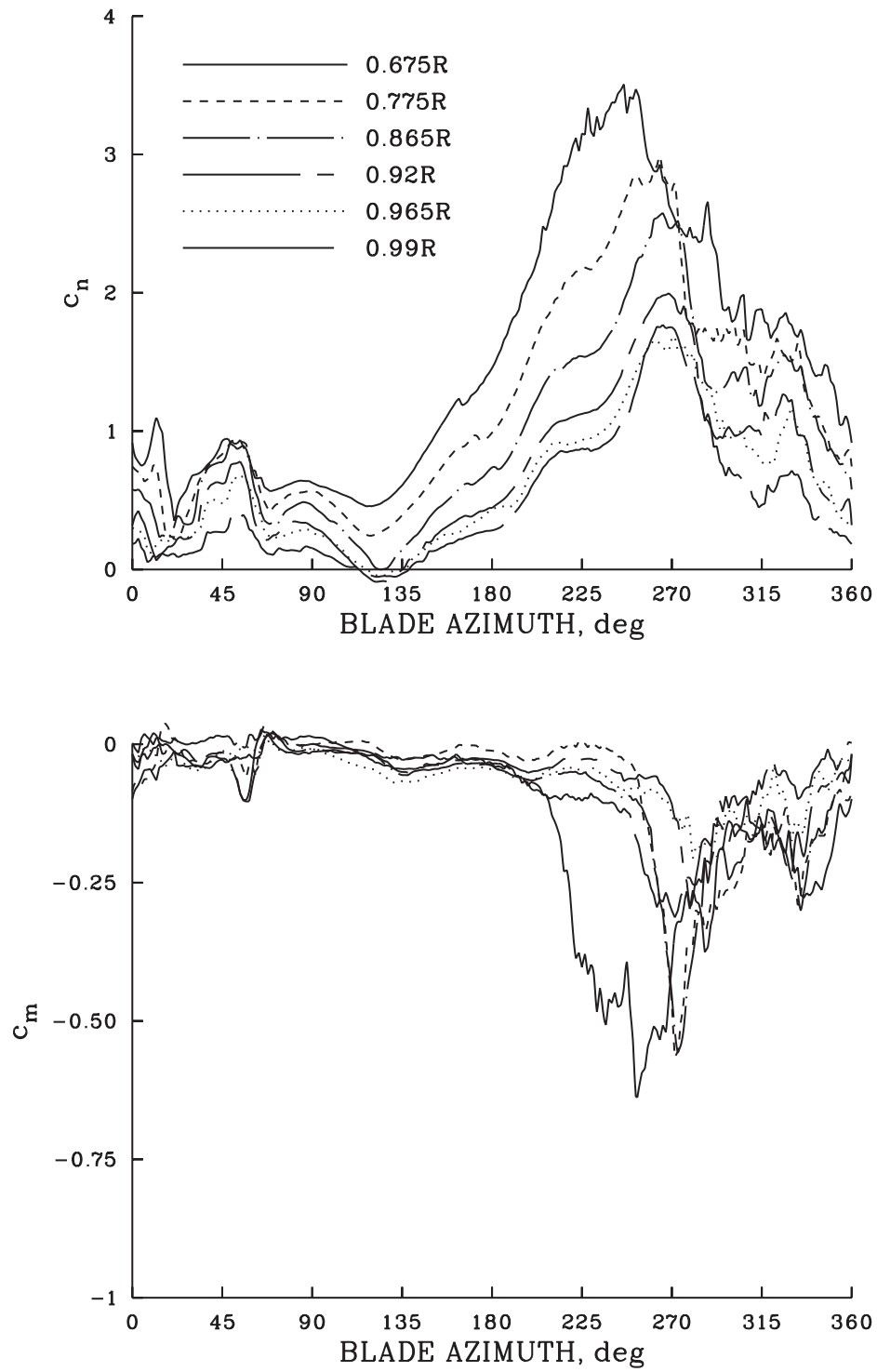


Figure 31. Normal force and moment coefficients on UH-60A rotor blade during UTTAS pull-up.

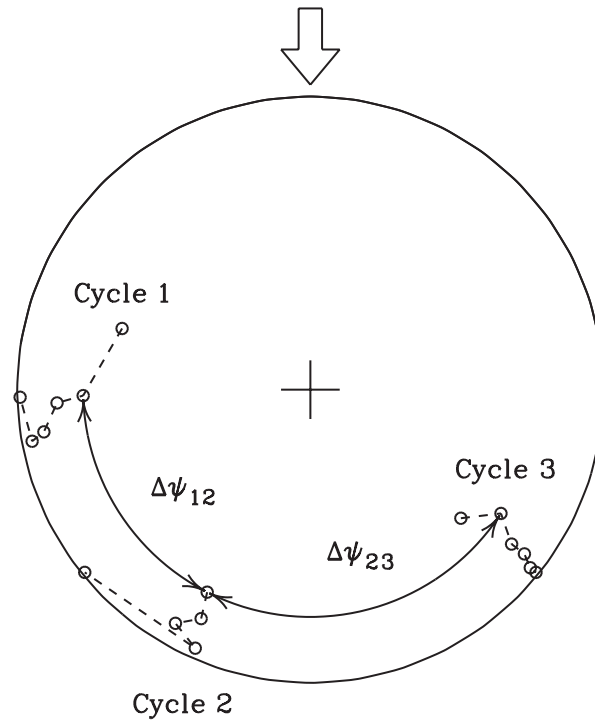


Figure 32. Schematic showing dynamic stall on UH-60A rotor for Rev 14.

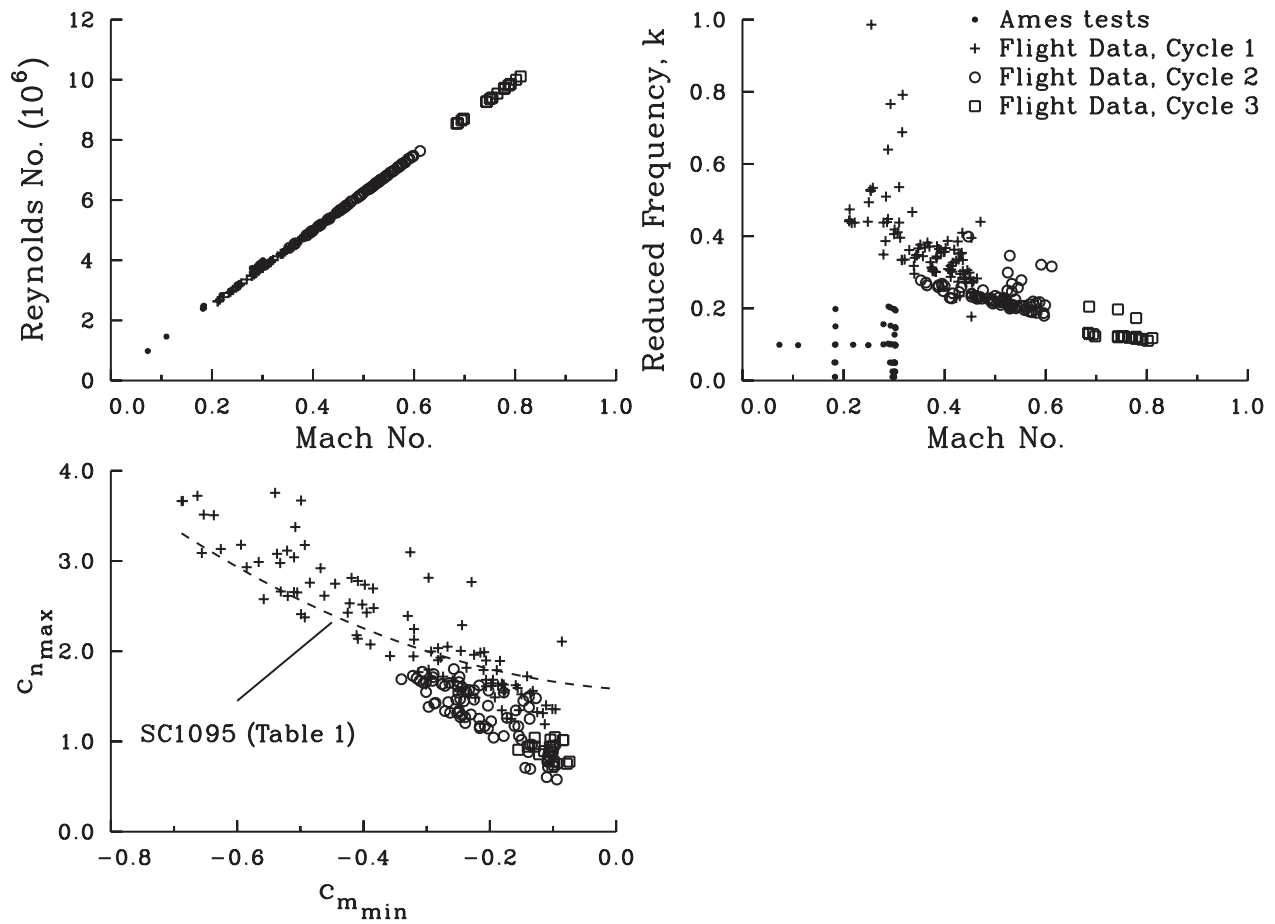


Figure 33. Comparison of UH-60A flight test normal force and moment coefficients with Ames SC1095 test results.

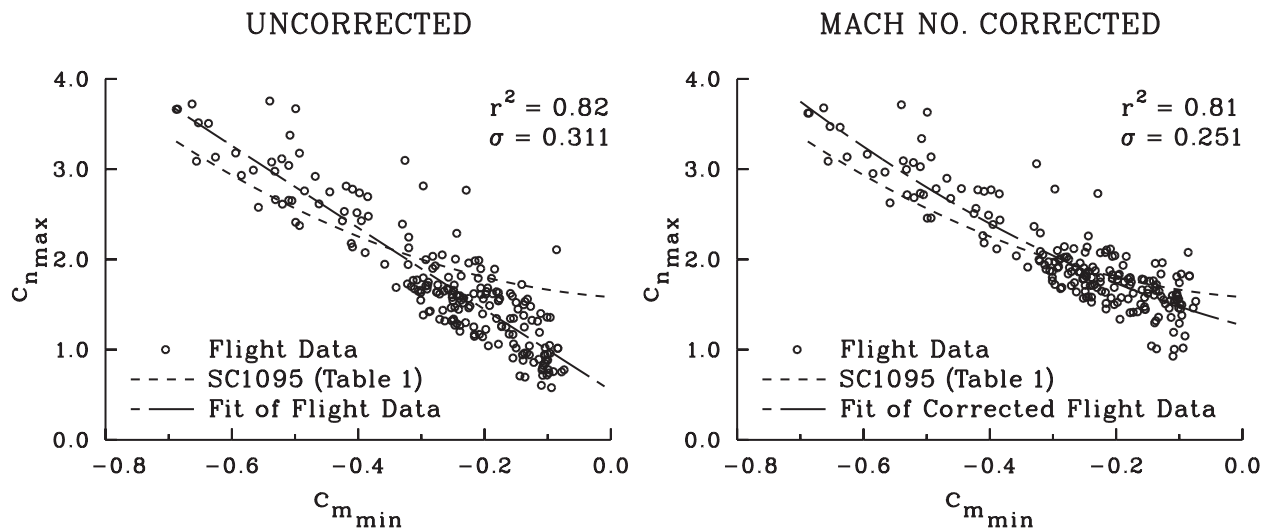


Figure 34. Effect of Mach number corrections on dynamic stall function obtained in flight.



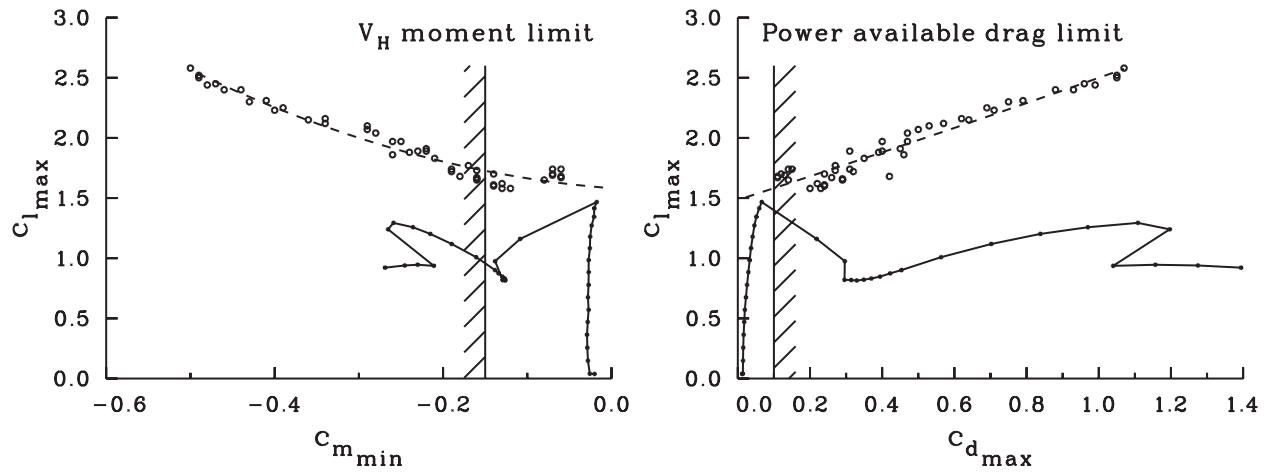


Figure 35. Dynamic and steady airfoil limits and design boundaries for the SC1095 airfoil.

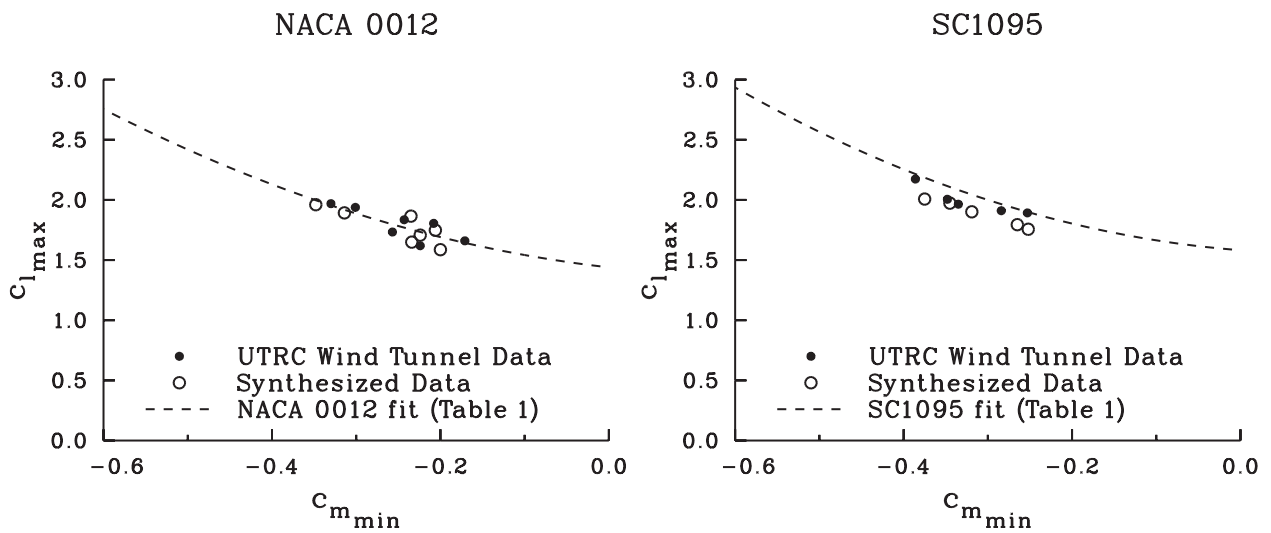


Figure 36. Comparison of measured and synthesized data for maximum lift and minimum moment for two airfoils (Ref. 17).

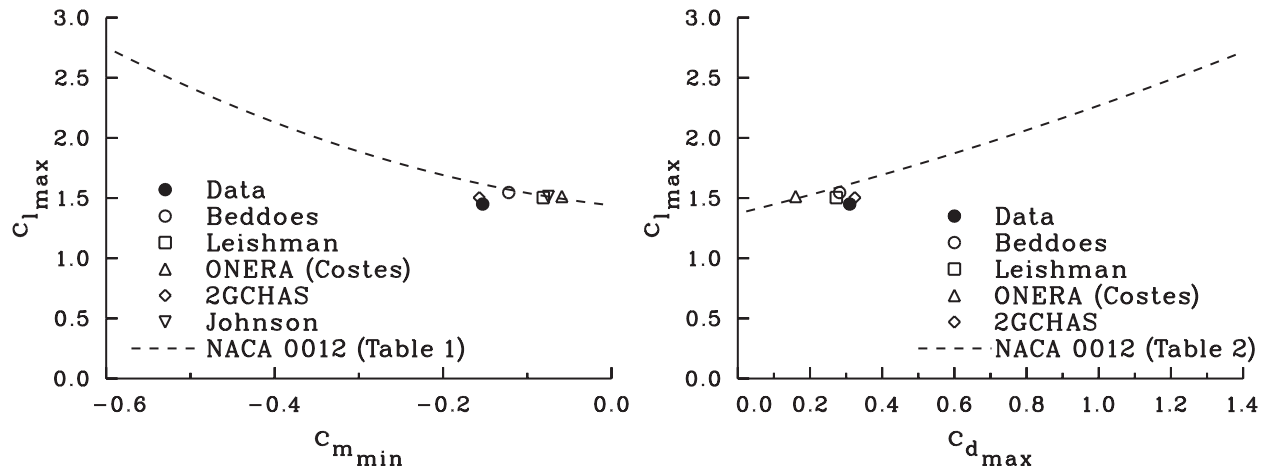


Figure 37. Comparison of synthesized data for NACA 0015 wing with five semi-empirical models (Ref. 30)..

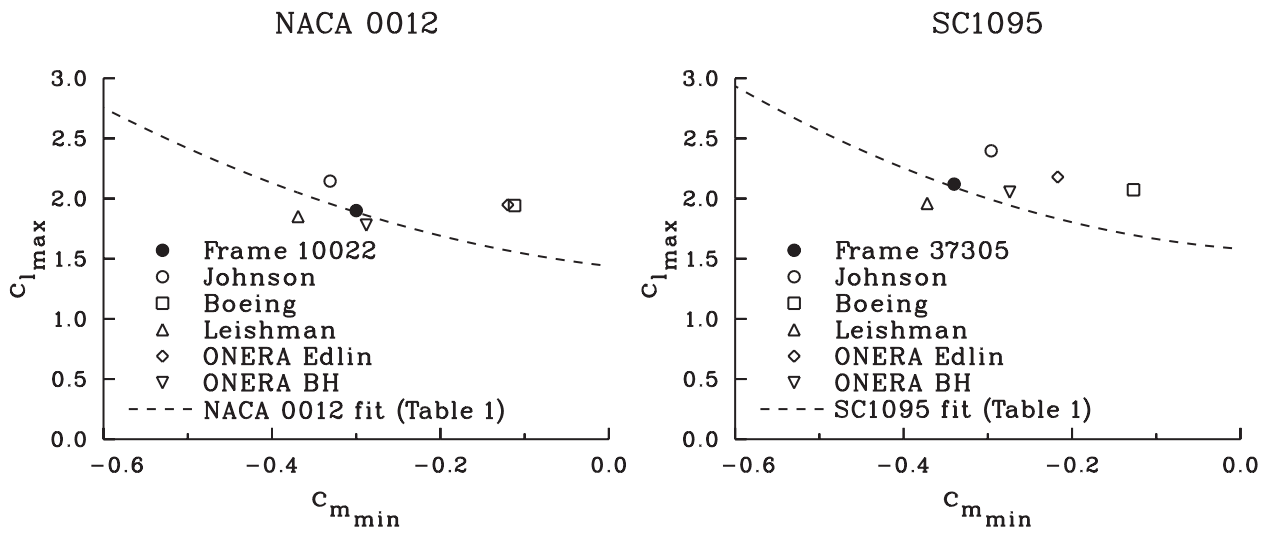


Figure 38. Comparison of synthesized data for NACA 0012 and SC1095 profiles using five semi-empirical models (Ref. 38).

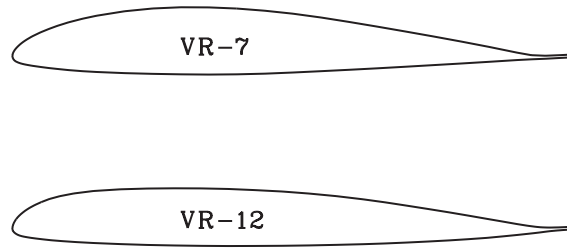


Figure 39. VR-7 and VR-12 profiles.

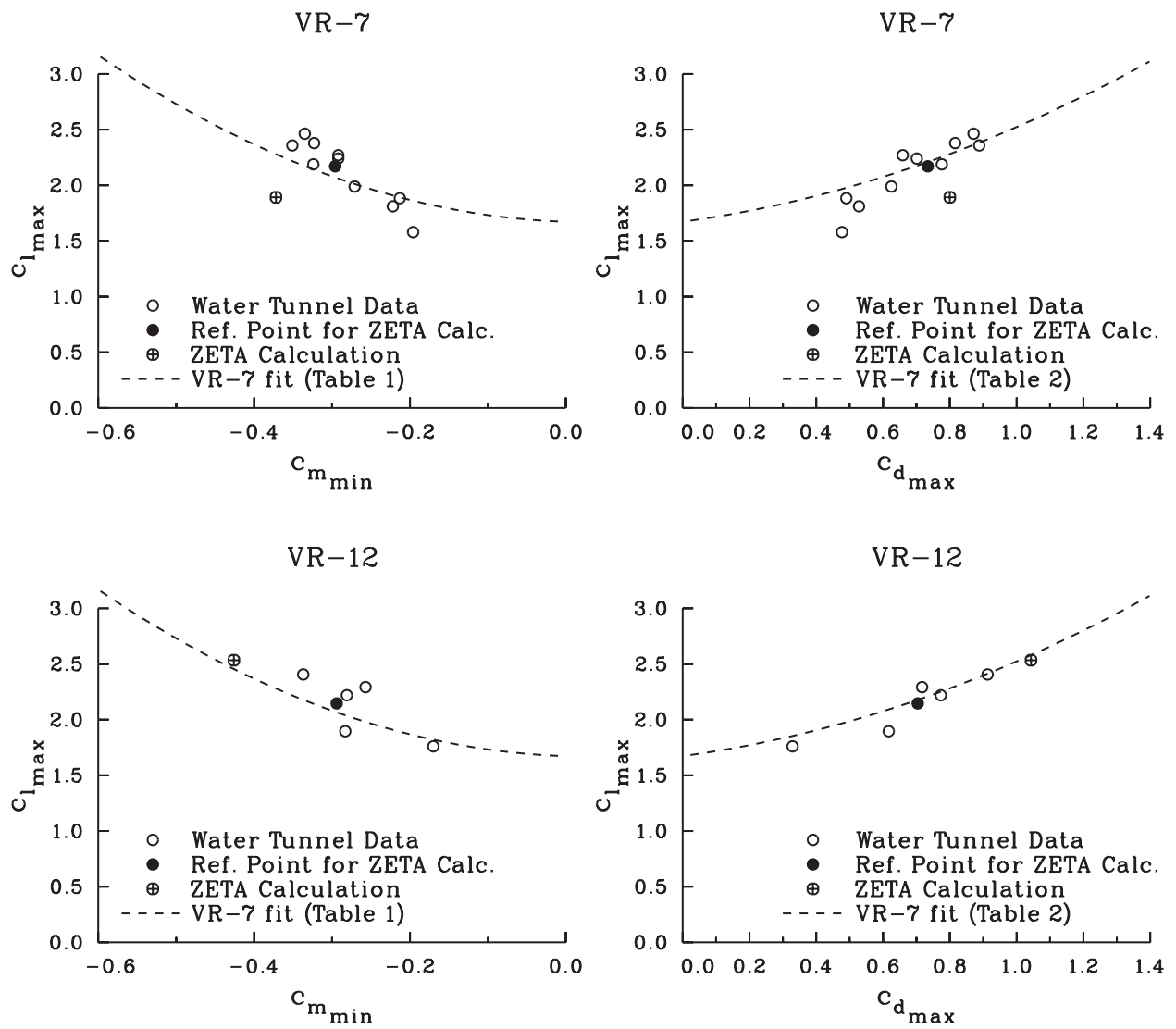


Figure 40. Comparison of ZETA code predictions for VR-7 and VR-12 airfoils (Refs. 43, 44).

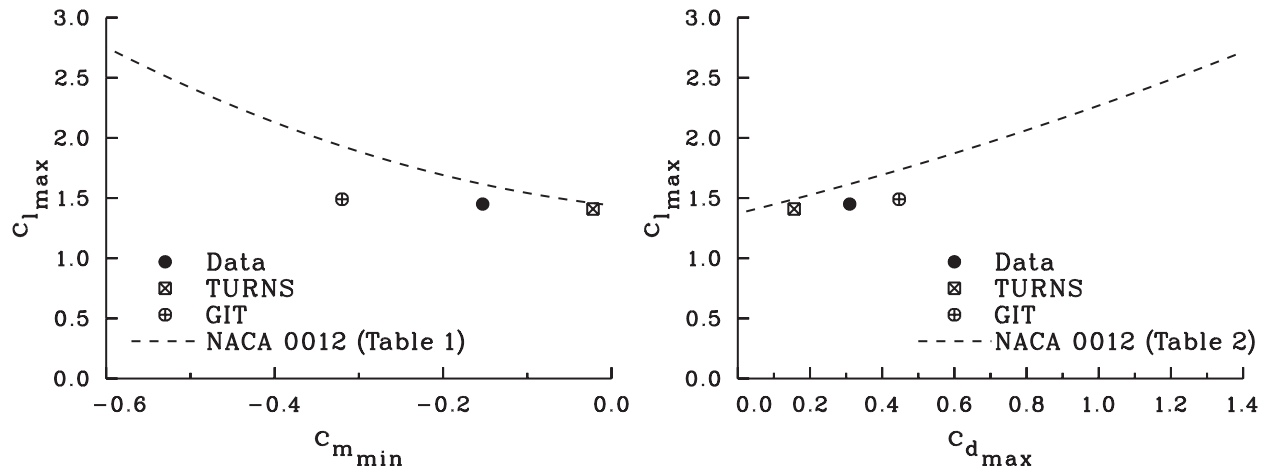


Figure 41. Comparison of Navier-Stokes predictions for NACA 0015 wing with experimental data (Ref. 30).

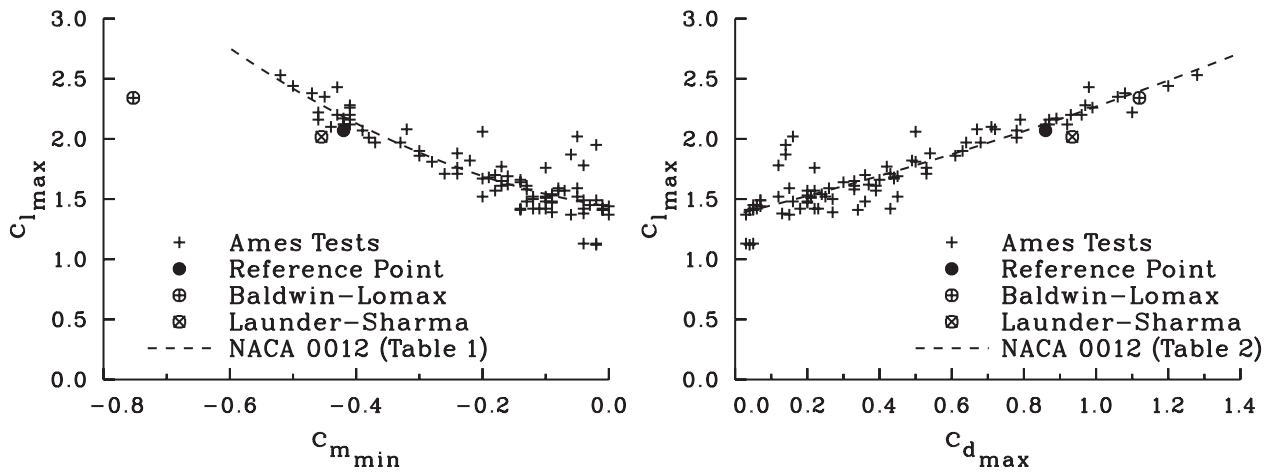


Figure 42. Comparison of Navier-Stokes predictions for NACA 0012 airfoil data using two turbulence models (Ref. 47).

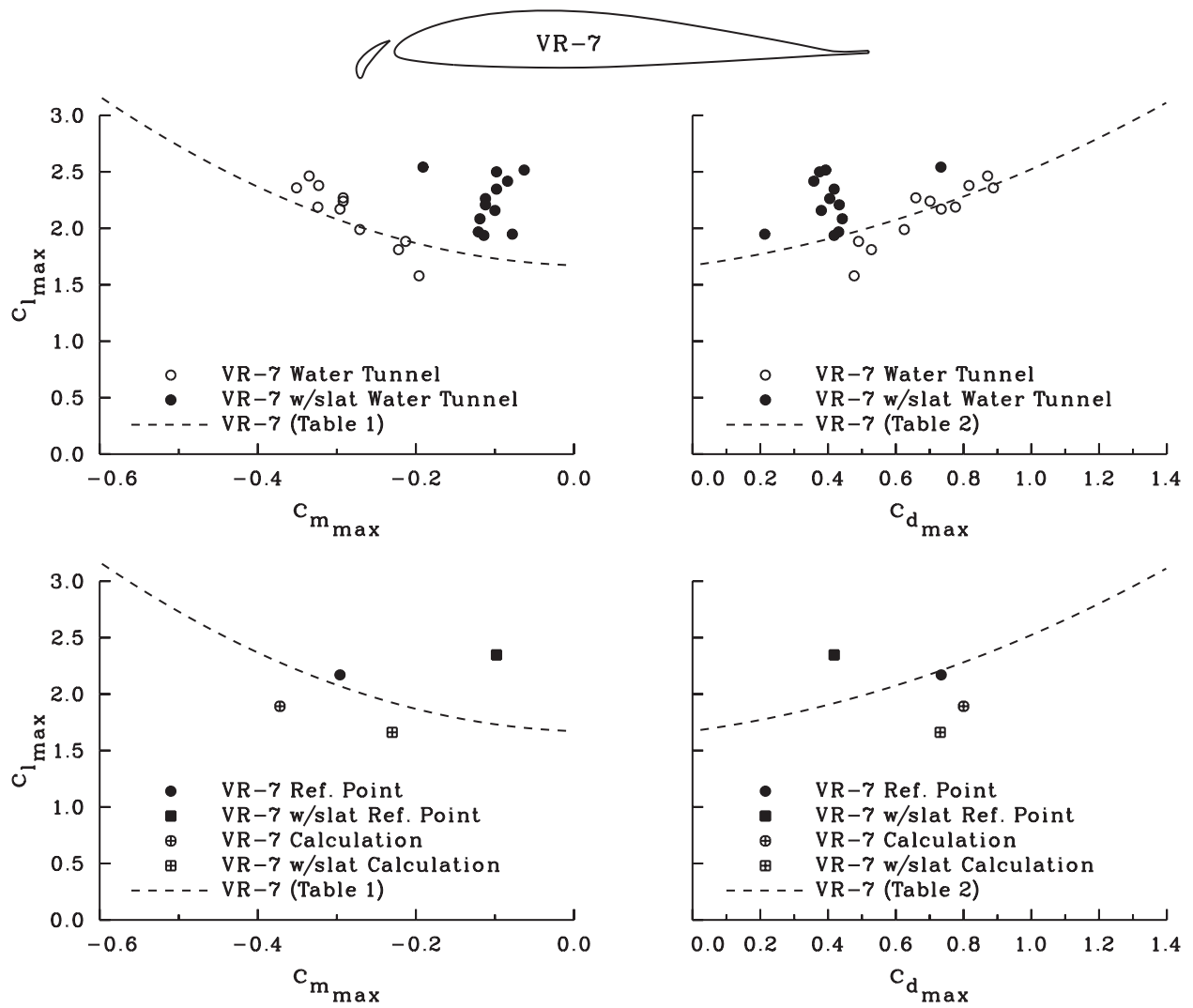


Figure 43. Comparison of experimental measurements and calculations for a VR-7 with and without a leading-edge slat. (Refs. 43, 44).

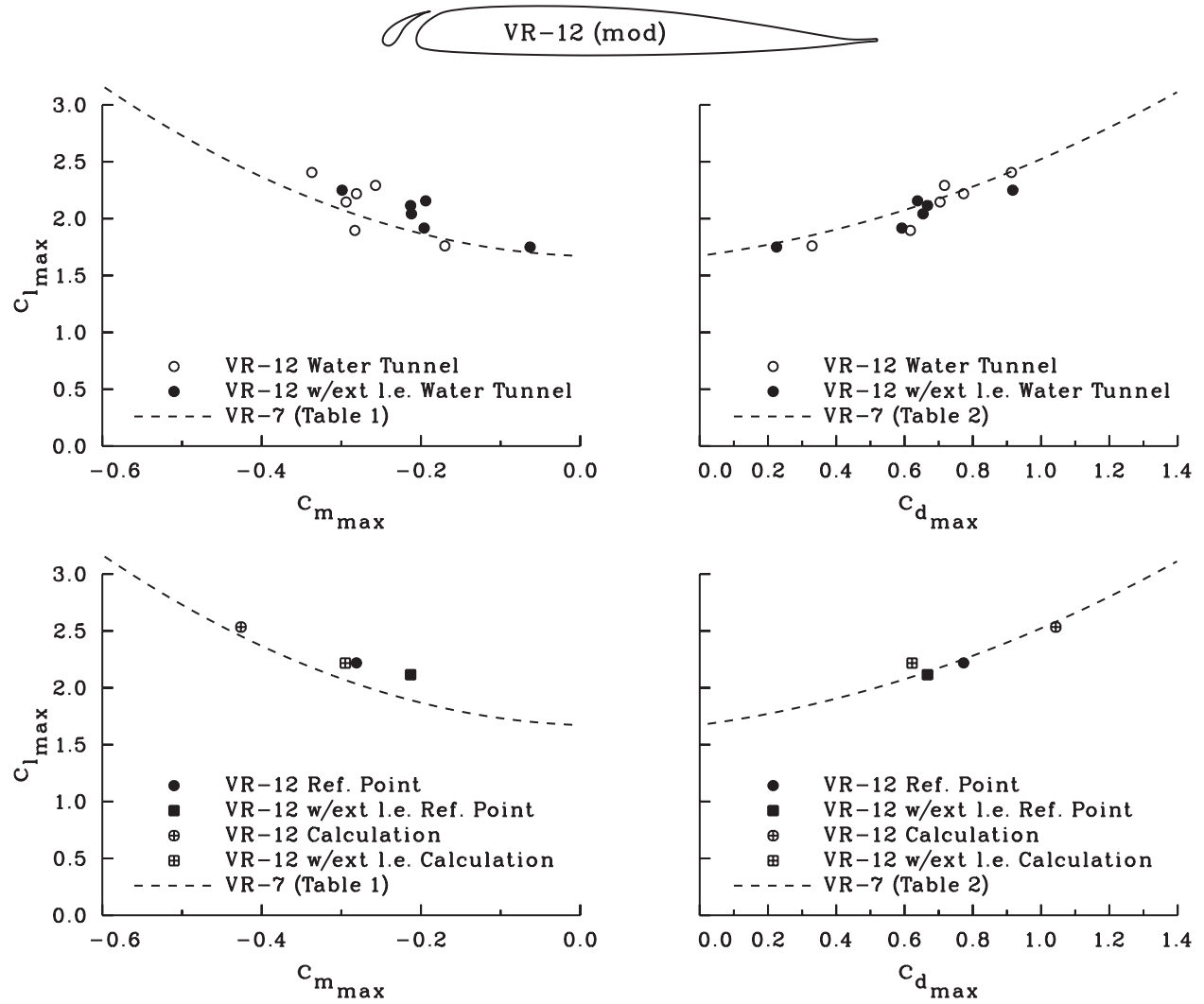


Figure 44. Comparison of experimental measurements and calculations for a VR-12 with and without a leading edge extension (Ref. 44).

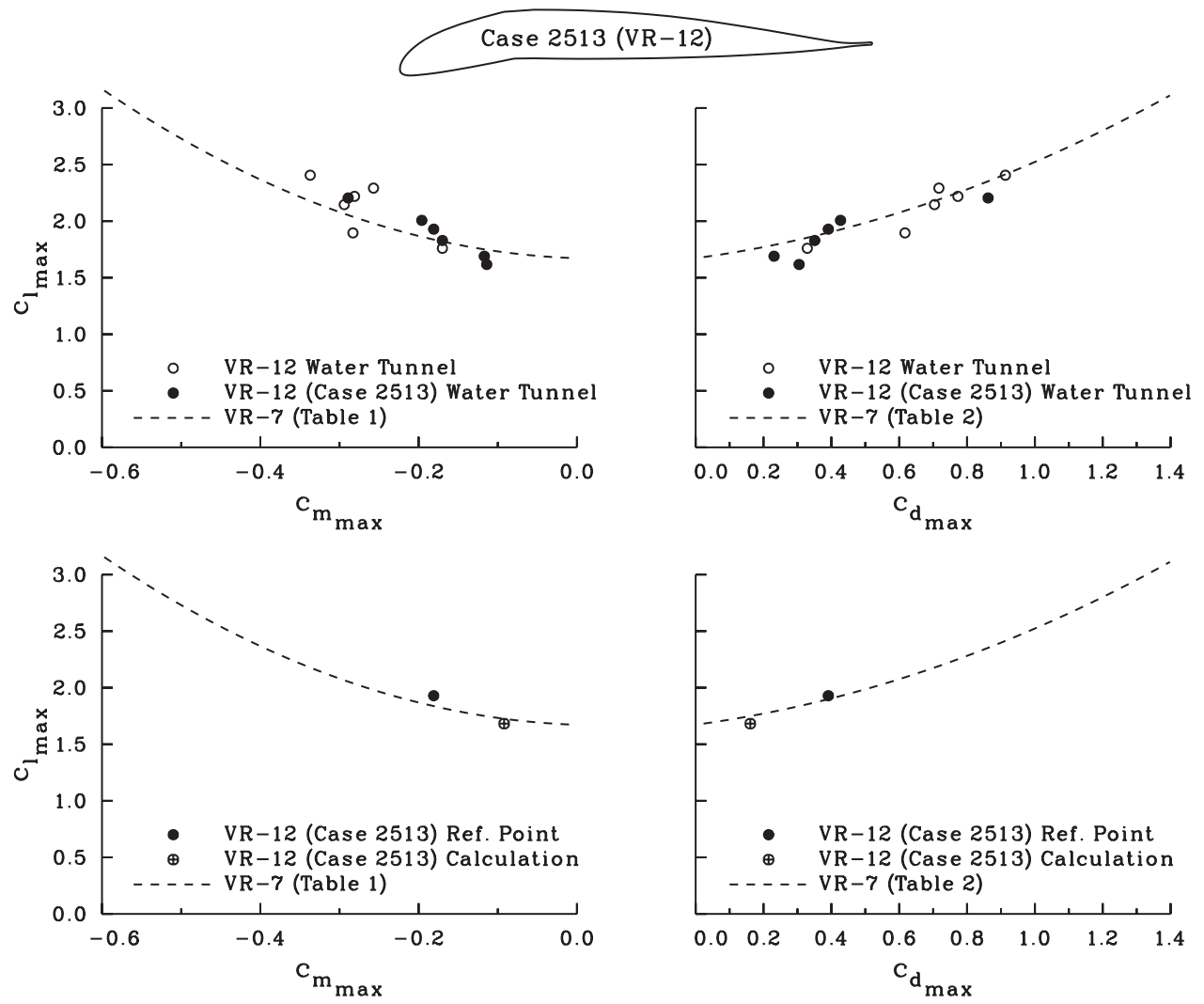


Figure 45. Comparison of experimental measurements and calculations for a VR-12 with a drooped leading section. (Ref. 48).

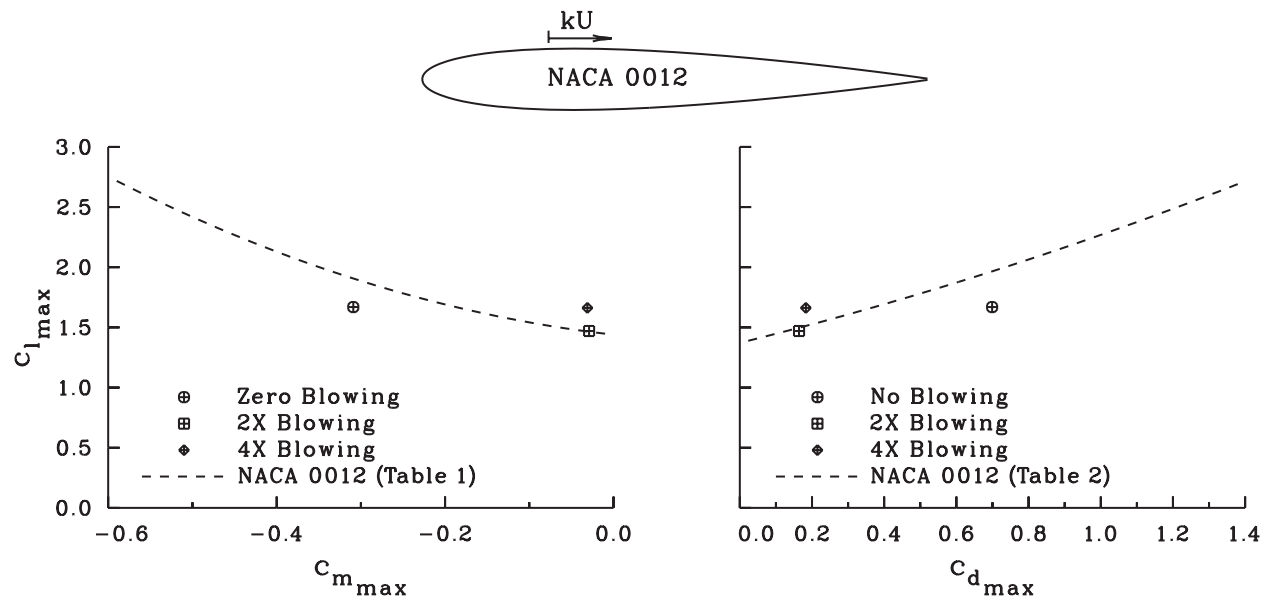


Figure 46. Calculated effects of blowing on an NACA 0012 airfoil. (Ref. 43).